An integrated geochemical spatial and temporal survey of thermal springs to characterize the geothermal resource of a volcano (Piton des Neiges, Réunion Island)

Bhavani Bénard, Vincent Famin, Bernard Sanjuan, Françoise Vimeux, Bertrand Aunay, Pierre Agrinier, Geneviève Lebeau

Journal Pre-proof

An integrated geochemical spatial and temporal survey of thermal springs to characterize the geothermal resource of a volcano (Piton des Neiges, Réunion Island)

Bhavani Bénard, Vincent Famin, Bernard Sanjuan, Françoise Vimeux, Bertrand Aunay, Pierre Agrinier, Geneviève Lebeau

PII: S0883-2927(23)00134-8

DOI: https://doi.org/10.1016/j.apgeochem.2023.105689

Reference: AG 105689

To appear in: *Applied Geochemistry*

Received Date: 6 December 2022

Revised Date: 4 May 2023

Accepted Date: 8 May 2023

Please cite this article as: Bénard, B., Famin, V., Sanjuan, B., Vimeux, Franç., Aunay, B., Agrinier, P., Lebeau, Geneviè., An integrated geochemical spatial and temporal survey of thermal springs to characterize the geothermal resource of a volcano (Piton des Neiges, Réunion Island), *Applied Geochemistry* (2023), doi: https://doi.org/10.1016/j.apgeochem.2023.105689.

An integrated geochemical spatial and temporal survey of thermal springs to characterize the geothermal resource of a volcano (Piton des Neiges, Réunion Island)

Bhavani Bénard[a, b, c], Vincent Famin[a, b], Bernard Sanjuan[c], Françoise Vimeux[d, e], Bertrand Aunay[f], Pierre Agrinier[a], Geneviève Lebeau[a, b]

[a] Université de Paris, Institut de Physique du Globe de Paris, CNRS, F-75005 Paris, France
[b] Université de La Réunion, Laboratoire GéoSciences Réunion, F-97744 Saint Denis, France
[c] BRGM, F-45060 Orléans, France
[d] HydroSciences Montpellier (Univ. Montpellier, CNRS, IMT, IRD), UMR 5151, 34095 Montpellier, France
[e] Institut Pierre Simon Laplace (IPSL), Laboratoire des Sciences du Climat et de l'Environnement (LSCE), UMR 8212 (CEA, CNRS, UVSQ), 91191 Gif-sur-Yvette Cedex, France
[f] BRGM, F-97400 Saint-Denis, La Réunion, France

Highlights

The heat source of hydrothermal waters is one of the volcanic rift zones.

There are two independent hydrothermal reservoirs on the northern and southern sides of the volcano.

Recharge of the two hydrothermal systems is plurennial and mostly fed by cyclones.

Geothermometry yields water-rock interaction temperatures of up to 141 ± 15°C.

The southern side of the volcano is the most promising target for future exploitation.

Coupling spatial and temporal geochemical information is useful for the geochemical exploration of hidden geothermal systems.

Abstract

Geothermal exploration can be challenging in the absence of obvious surface indicators of a high enthalpy geothermal resource such as geysers, fumaroles or thermal springs with temperatures near 100°C. This is the case at the Piton des Neiges volcano (Réunion Island), which displays evidence of hydrothermal activity mostly as thermal springs with temperatures not exceeding 50°C, affected by mixing and reequilibration, and emerging in a complex geological framework, resulting from the polygenic history of this dormant volcano. Yet, these thermal springs keep a partial record of the reservoir geochemistry. Here, we propose an exploration method to set this thermal signature apart from the contribution of other processes and trace back the equilibrium conditions, enabling us to locate thermal fluid circulations, and evaluate their temperature and availability. We report its application at Piton des Neiges volcano. We led an extensive geochemical survey which nearly doubled the number of thermal springs reported on the volcano and dramatically extended the existing geochemical database in space and time. In tandem, we also monitored $\delta^{18}O$ and δD values in rainwaters and thermal springs over two years to compare their temporal variations.

Our surveys show that the repartition of thermal springs is controlled by only one of the volcanic rift zones (the N30°E axis), which is thus identified as the heat source of hydrothermal circulations. This N30°E rift zone is also a preferential pathway for the degassing of mantellic CO_2. In addition, the composition of thermal waters is influenced by syenite intrusions along the rim of the caldera, acting as drains for the uprise of hydrothermal waters. O, H and Sr isotopic signatures of springs show that the geothermal resource of Piton des Neiges is in fact made of two independent and unconnected hydrothermal systems on the northern and southern circular depressions of the volcano (the cirques of Salazie and Cilaos, respectively). Their recharge is meteoric, multi-year, and mostly achieved by cyclonic events. Thermal waters experience reequilibration during their ascent and various degrees of CO_2 input or degassing. Last equilibrium temperatures of water/rock interaction, estimated by multicomponent geothermometry, reach up to 125 ± 6°C in the cirque of Salazie, and up to 141 ± 15°C in the cirque of Cilaos, with possibility for hotter waters before reequilibration. Taken together, our results suggest that the most promising target for future exploration is located in the cirque of Cilaos, along the caldera rim, and in proximity of syenite intrusions.

With a thorough prospecting of thermal springs, a comprehensive geochemical study and a geochemical monitoring of the different water reservoirs, we improved our understanding of the geothermal resource and identified future exploration targets at Piton des Neiges volcano.

Keywords

Geothermal ; Exploration ; Geochemistry ; Piton des Neiges ; Volcano ; Thermal springs

Introduction

Geothermal energy is a renewable energy source with little emission of carbon dioxide to the atmosphere and thus well suited to climate change mitigation. However, geothermal exploration can be challenging in the absence of obvious surface indicators of a high enthalpy geothermal resource such as geysers, fumaroles or thermal springs with temperatures near 100°C. Yet, these “hidden” systems can represent the majority of the geothermal potential resource (e.g. in the U.S.A., Williams et al., 2009). In order to address this issue, several methods are in development to assess their geothermal potential such as statistical analysis (e.g. in Hawaii, Lautze et al., 2017b, 2017a), machine learning (e.g. in the U.S.A., Vesselinov et al., 2021), or 3D magnetotelluric surveys (e.g. in La Palma, Canaries, Di Paolo et al., 2020). Most of the time, these systems still display some evidence of hydrothermal activity, often in the form of non-boiling thermal waters, which can represent a supplementary exploration tool. This type of manifestation is especially common on mature and polygenic volcanoes, for example as groundwaters with thermal anomalies in the islands of Maui and Lanai, Hawaii (Lautze et al., 2017a), or as thermal springs on the Taburiente volcano in La Palma, Canaries (Troll and Carracedo, 2016) and in Quaternary and Tertiary formations of western Iceland (Arnórsson, 1995). However, polygenic volcanoes are by essence made of multiple eruptive periods, quiescent phases and destabilization episodes. This history results in complex internal architectures, which affect the geometry of thermal water circulation as well as the location, depth, and nature of the heat sources and the permeability of rocks (e.g. at Mount Meager in British Columbia, Grasby et al., 2019), making the use of thermal springs for geothermal exploration challenging.

Réunion Island is a good example of a polygenic volcanic island offering potential for geothermal energy, but where exploitation is hampered by a lack of geological knowledge on the hydrothermal systems (see review by Dezayes et al., 2022). Piton des Neiges volcano displays evidence of hydrothermal activity, in the form of thermal springs (up to 48°C), fumarole deposits, and CO_2 – He –

Rn anomalies (Marty et al., 1993; Rançon and Rocher, 1985; Sanjuan et al., 2001). This volcano also hosts several geophysical indicators in favor of a geothermal resource (Dezayes et al., 2022). Moreover, two exploratory boreholes revealed the existence of elevated temperature gradients (180°C/km and 82°C/km) on this dormant volcano. All these lines of evidence confirm the presence of a heat source and of hot water circulation, which may be suitable for the development of geothermal energy on the island. However, exploratory drillings made so far did not reach zones of sufficient permeability to allow an exploitation of hot water (Augé et al., 1989; Demange et al., 1989). More geological information is needed to locate fluid circulations in this dormant volcano, assess the resource represented by its hydrothermal system, and define the most promising targets for future exploration.

In a previous paper, we proposed a conceptual model for the Piton des Neiges hydrothermal system in a first study (Bénard et al., 2020). Based on the chemical and isotopic composition of 17 thermal springs, we determined the different mineralization processes responsible for their geochemical profiles. We found that thermal waters are of meteoric origin, subject to CO_2 dissolution from a degassing magma, to water-rock interaction with either basalts or differentiated rocks which increase their total mineral content, and some samples also showed a contamination from elements originating from seawater. With the knowledge of the processes involved in the mineralization of thermal waters, the aim of the present work is to characterize the geothermal resource and estimate its temperature. For this purpose, we led an extended field prospection and sampling, which includes waters displaying field evidence of a thermal component and rocks from different geological units. We used physiochemical parameters, major element concentrations, and CO_2 partial pressure (PCO_2) computations to highlight the zones displaying the most promising geothermal resource. In order to better understand the hydrogeological characteristics of the aquifer systems with which thermal waters are mixed, we studied the spatial distribution of Cl, $\delta^{18}O$ and δD in waters and that of $^{87}Sr/^{86}Sr$ in waters and rocks. To refine our understanding of aquifer recharge, we monitored the monthly isotopic composition ($\delta^{18}O$, δD) of rain and thermal springs over two years. We then applied the most up-to-date thermodynamic-based geothermometry tools (Cioni and Marini, 2020; Spycher and Finsterle, 2016) to reconstruct the temperature history of the geothermal fluids. This work leads to a considerably improved model of hydrothermal circulation at Piton des Neiges, which may be used to target zones where the geothermal resource is most likely present and to plan the next steps of geothermal exploration. Our methodology of geochemical investigation may be exported to any other volcano with thermal springs mixing with superficial waters.

1. Geological and hydrogeological settings

Réunion Island was formed by two main volcanoes: Piton des Neiges and Piton de la Fournaise. Piton des Neiges, presently dormant, is the oldest and the largest edifice. Piton de la Fournaise, still active, grows on the south-eastern flank of Piton des Neiges. Estimated to have emerged at 3 Ma ago, Piton des Neiges has a polygenic history of at least five eruptive periods separated by quiescence and erosion intervals. The shield building stage of this volcano has produced transitional basic magmas until 430 ka (Kluska, 1997; McDougall, 1971). After a 80 ka period of rest, the volcano entered into a degenerative stage 350 ka ago and produced alkali differentiated magmas ever since (Gillot and Nativel, 1982; Kluska, 1997). The last known eruption of Piton des Neiges dates back to 27 ka (see review by Famin et al., 2022). This last period of quiescence, and the heavy rainfalls under tropical climate, have favored erosion of the volcanic edifice, now incised by three cirques (subcircular depressions), Salazie to the north, Mafate to the northwest, and Cilaos to the south (Figure 1). These deep cirques have dissected the inner structure of the volcano, erasing most of the surface evidence of calderas. Based on patchy observations of faults, offset lava layers, pyroclastic deposits or radial dykes, two calderas have been proposed (Figure 1): a large one running through the three cirques

formed during the differentiated stage (210 – 180 ka), and a smaller one in the summit area of Piton des Neiges formed during its last activity (Chevalier, 1979; Rocher, 1988).

Erosion has exposed the hypovolcanic complex, made of dense gabbroic plutons and basaltic, trachytic and syenitic planar intrusions. Planar intrusions are organized into two rift zones N30°E and N110-160°E, and two sill zones between 800 and 1300 m above sea level (Chaput et al., 2017, 2014). The two deep boreholes SGTH-1 (201 m) and SLZ1 (2108 m) drilled for geothermal exploration in the 1980s (Chovelon, 1986; Gérard and Stieltjes, 1979) intersect a pluri-kilometric gabbroic intrusive complex, associated with the shield building stage of Piton des Neiges. The high geothermal gradients (respectively of 180°C/km and 82°C/km) obtained in these boreholes show that heat issued from volcanic activity is still being transmitted into the massif. However, both boreholes were dry and the nature of the heat source (either the gabbro pluton or the planar intrusions) remains unknown. Syenite intrusions, which consist in 30 – 100 m thick dykes in the cirques of Salazie and Cilaos, are of particular interest for this study. Ages of less than 150 ka, they represent major dyke structures of the terminal volcanic activity (Famin et al., 2022), located within the N30°E rift zone, and interpreted to delineate the largest caldera (Chevalier, 1979; Rocher, 1988). Additionally, many thermal springs are observed in these intrusions or in their immediate vicinity. All these criteria suggest that syenite intrusions represent a candidate heat source for the hydrothermal system, or at least act as conduits for hot fluid flow (Bénard et al., 2020; Frissant et al., 2003; Sanjuan et al., 2001).

Fluid circulation in the edifice is complexified by its long history of construction, destruction, intrusive activity and secondary mineral precipitation. Indeed, the hypovolcanic complex of Piton des Neiges is affected by several phases of low-grade metamorphism and hydrothermal alteration (Chevalier, 1979; Rançon, 1985), resulting in a porosity clogging by secondary precipitation of phrenite-pumpellyite facies minerals in rocks of the shield-building stage, followed by carbonate precipitation in differentiated rocks as well as in mafic rocks (Famin et al., 2016). The ensued low hydraulic conductivity, associated with the geological barriers formed by planar intrusions, limit the escape of freshwater toward the sea and its downward infiltration in the lowermost, oldest and most impermeable rock units (Join et al., 2005). Thermal waters, accordingly, is mostly fed by meteoric water (Bénard et al., 2020). The tropical climate of Réunion Island consists in a dry season (April-November), and a wet season (December-March) that delivers huge precipitation rates (annual mean of ~2500 mm in the cirques). Most of these wet season rainfalls occur as cyclones or tropical storms (five events per year in average for the period 1981 – 2010; Jumaux et al., 2011).

Despite the present-day inactivity of Piton des Neiges, there is still evidence of magmatic degassing from a deep mantle source on a regional scale (Boudoire et al., 2017). Magmatic carbon dissolves in large quantities in the hydrothermal system (Bénard et al., 2020; Marty et al., 1993; Trull et al., 1993). Fumarolic sulfur deposits are also observed, but it is unknown whether they are fossil or still active (Lopoukhine and Stieltjes, 1978; Rançon and Rocher, 1985).

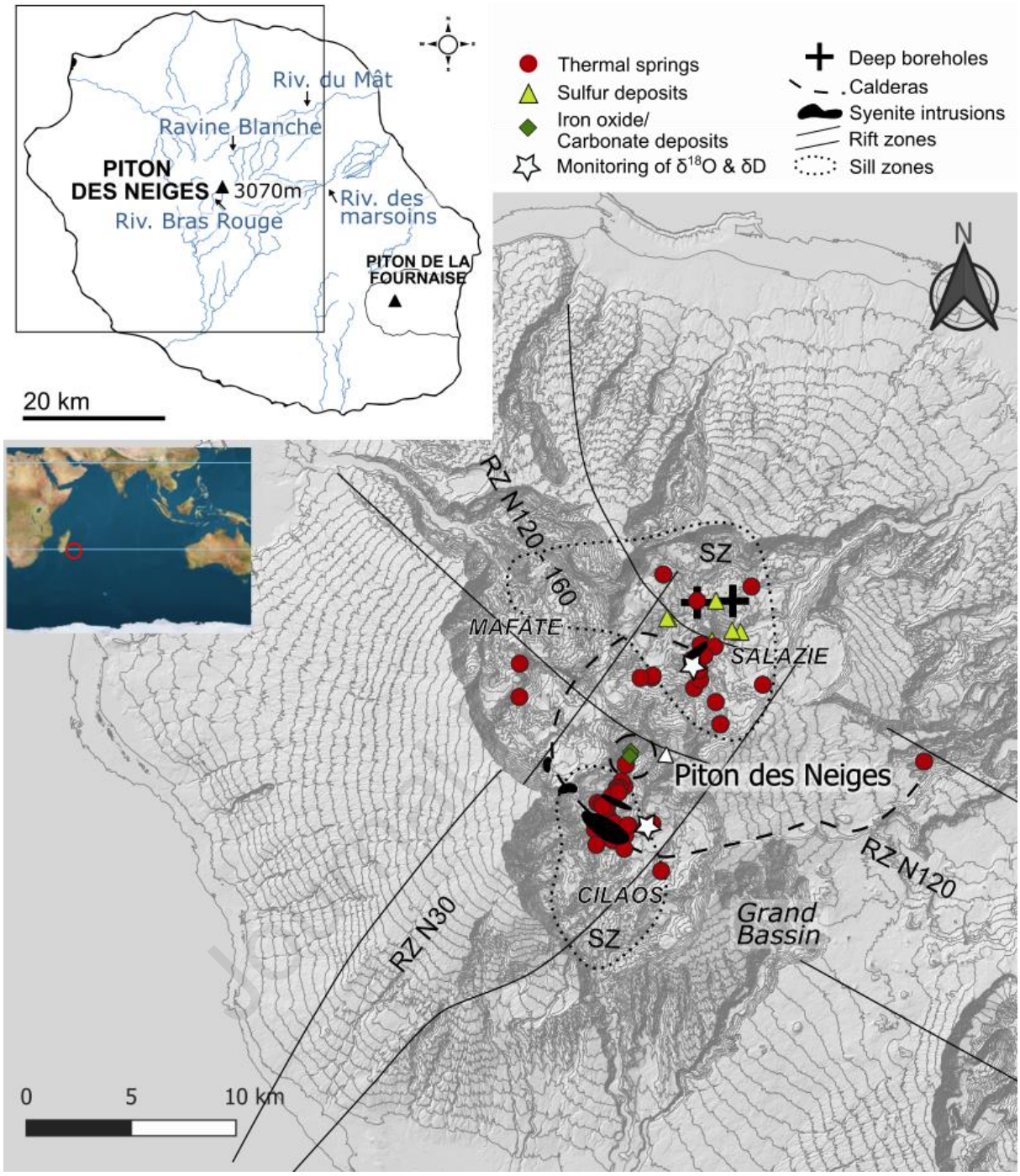

Figure 1: Localization of the field indicators of hydrothermal activity in Piton des Neiges: thermal springs, iron oxide deposits, carbonate deposits and sulfur deposits from previous studies (Aunay et al., 2013; Belle, 2014; Bénard et al., 2020; Frissant et al., 2003; Iundt et al., 1992; Lopoukhine and Stieltjes, 1978; Louvat and Allègre, 1997; Sanjuan et al., 2001), the main rift zones (RZ) and sill zones (SZ) of Piton des Neiges (Chaput et al., 2017), the two supposed calderas (Chevalier, 1979; Rocher, 1988), the two deep boreholes drilled for geothermal exploration in the 1980s (Chovelon, 1986; Gérard and Stieltjes, 1979), the two monitoring sites of $\delta^{18}O$ and δD in springs and rain. Relief contours at 100 m intervals from RGE ALTI® - IGN.

2. Material and Methods

2.1. Fieldwork and sampling

We led an extensive prospection on the field to identify all indicators of hydrothermal activity and measure and sample new thermal springs. Springs were considered as an indicator of hydrothermal activity whenever they displayed at least two of the following criteria:

- Presence of iron oxide/carbonate/sulfide deposits,
- A higher temperature (≥ 5°C) compared to nearby river water at the time of sampling,
- A higher electrical conductivity (EC) (≥ 200 µS/cm) compared to nearby river water at the time of sampling,
- A lower pH (≤ 1) compared to nearby river water at the time of sampling.

Temperature, EC, and pH were measured at the outlet and EC was normalized at 25°C.

In total, our spatial and temporal sampling campaign yielded a set of 130 water samples. The first spring samples were taken during an exploratory phase in June 2015, hereafter referred to as "the first phase". All the others spring samples were taken over a long period lasting from December 2015 to May 2019, hereafter referred to as "the second phase".

Thermal springs were sampled to be analyzed for major elements, Al, Sr, and Br concentrations and $\delta^{18}O$, δD, $\delta^{13}C$ and $^{87}Sr/^{86}Sr$ isotopic ratios. Thermal springs displaying particularly interesting or intriguing features were sampled several times. The three large rivers Bras Rouge in Cilaos, Rivière du Mât and Ravine Blanche in Salazie were also sampled at the highest possible altitude for analysis of $\delta^{18}O$ and δD isotopic ratios in order to give reference points for river waters, respectively at 2050, 1830 and 1739 m. We also sampled several rocks from the late activity of Piton des Neiges – and thus the most likely to produce heat – in order to compare their strontium isotopic signature to that of thermal springs.

For all the samples, water was filtered at 0.2 µm on site. Bottles were rinsed three times with filtered water before sampling. Bottle caps were sealed with parafilm. For the analysis of major and trace elements, and $^{87}Sr/^{86}Sr$ isotopic ratios, water samples were collected in LDPE bottles. Water samples for analysis of major cations, Al, Sr, and Br concentrations and $^{87}Sr/^{86}Sr$ isotopic ratios were acidified with acid (HNO_3 0.3N) on site. However, for the samples of the second phase, there was too little acid to prevent calcite precipitation in the bottles, which resulted in erroneous values for the concentrations of Ca and Sr for 17 samples, which were displayed in Bénard et al., (2020). For the purpose of this study, we added back acid to unused samples from the second phase and re-analyzed them for cations and trace elements. For $\delta^{18}O$ and δD analyses, water was sampled 15 mL amber glass or HDPE bottles with no headspace. During the second phase, water samples were also collected for analysis of total dissolved inorganic carbon content (TDIC) and $\delta^{13}C$ in Labco 12 mL Exetainer vials with no headspace.

Additionally, we monitored rainwater and thermal springs time fluctuations on two sites from April 2017 to May 2019. On a monthly basis, we collected water from two thermal springs in each cirque (Trou Blanc Amont – TBA – in Salazie and Irénée – IRN – in Cilaos, Figure 1) and from rainwater collectors installed nearby these two springs (at elevations 910 m and 1120 m respectively) for analysis of $\delta^{18}O$ and δD isotopic ratios. Springs IRN and TBA were also analyzed for major and trace elements. These two springs were selected because of (i) their unambiguous hydrothermal signature (Bénard et al., 2020), (ii) their relatively easy access, and (iii) the possibility of installing rainwater collectors nearby. For the two rain collectors, rainwater was collected in a PEHD container through a funnel and trapped under a layer of liquid paraffin to prevent water evaporation. Each month, one sample was taken out of the total volume of water collected in a 15 mL bottle, made of amber glass with a cone-shaped cap or of HDPE with no headspace. As for thermal springs, water was filtered at 0.2 µm on site,

bottles were rinsed three times with filtered water before sampling and bottle caps were sealed with parafilm.

All the samples were stored at a temperature of 6°C before shipment.

2.2. Analysis

For the water samples of the first sampling phase, alkalinity, major/trace elements and $\delta^{18}O$, δD and $^{87}Sr/^{86}Sr$ isotopic ratios' analyses were performed at the Bureau de Recherches Géologiques et Minières (BRGM) in Orléans (France). For the water samples of the second sampling phase, total dissolved inorganic carbon (TDIC) and major elements analyses were performed at the Institut de Physique du Globe de Paris (IPGP). $\delta^{18}O$ and δD of thermal springs and precipitations were analyzed at the Laboratoire des Sciences du Climat et de l'Environnement (LSCE) in Saclay. Sr concentrations and isotopic ratios analyses on rocks were performed by the Service d'Analyse des Roches et des Minéraux (SARM-CRPG) in Nancy.

Major anions concentrations were determined by ion exchange chromatography (ICS1100 Thermofisher, column Ionpac thermo AS14 and precolumn Ionpac thermo AG14, column AS14 and precolumn AG14). Major cations concentrations were determined using inductively coupled plasma atomic emission spectrometry (ICP-AES, iCAP6200 Thermofisher). For the Ca and Sr concentrations of the 17 samples for which the previous analysis was inaccurate, we performed a new analysis using inductively coupled plasma mass spectrometry (ICP-MS, Agilent 7900). Al, Sr, and Br concentrations were determined by ICP-MS for the two phases. Precision for major cations and anions concentrations is < 5 % (except HCO_3, < 10 %, see below), and < 20 % for trace elements. Uncertainties were calculated using the standard deviation on measurement replicates and the uncertainty on the internal standard concentration.

For the water samples of the first phase, alkalinity was determined using potentiometric titration, giving HCO_3 concentrations with a quantification limit of 10 mg/L. For the water samples of the second phase TDIC and carbon isotope ratios $\delta^{13}C$ analyses were made by gas chromatography and isotope ratio mass spectrometry (GC-IRMS), after releasing TDIC as CO_2 by H_3PO_4 acidification (Assayag et al., 2006). For this phase, HCO_3 concentrations were computed using the temperature dependent acid dissociation constants from Mook and Koene, (1975), knowing the TDIC, temperature and pH of waters. However, this analysis method gave poor estimates of dissolved carbonate concentrations for the thermal springs with a high TDIC as 35 samples from the second phase yielded ionic balances > 5 %. For these 35 samples, HCO_3 concentrations had to be corrected and were estimated by setting the ionic balance to 0 %. $\delta^{13}C$ are expressed in per mil (‰) with respect to the PDB standard, with a precision of 0.1 ‰.

For the water samples of the first phase, $\delta^{18}O$ and δD of thermal spring and rivers were obtained by gas chromatography coupled to isotope ratio mass spectrometry (GC-IRMS), after equilibration with H_2 for hydrogen and CO_2 for oxygen, leading to an accuracy of 0.1 ‰ in $\delta^{18}O$ and 0.8 ‰ in δD. For the water samples of the second phase, $\delta^{18}O$ and δD were obtained using the CO_2-H_2O equilibration method on a Finnigan Mat 252 and the WS-CRDS infrared laser method respectively. $\delta^{18}O$ and δD are expressed in ‰ with respect to the VSMOW standard. The accuracies are of ± 0.05 ‰ and ± 0.7 ‰ for $\delta^{18}O$ and δD, respectively.

For the water samples of the first phase, $^{87}Sr/^{86}Sr$ ratios were determined by mass spectrometry using a triple multidynamic acquisition and a single W filament. For the water samples of the second phase,

strontium isotopic ratios $^{87}Sr/^{86}Sr$ were determined by multi-collector mass spectrometry (TIMS). Precisions are between 0.000006 and 0.000018.

Strontium isotopic ratios in rocks were determined by the Service d'Analyse des Roches et des Minéraux (SARM) of the Centre de Recherches Pétrographiques et Géochimiques (CRPG), Nancy, France. About 100 to 200 mg of sample were weighed in a 15 ml Savillex and digested using a solution of 14M HNO_3 (4 mL). The whole mixture was heated on a hot plate at 115°C for 24 - 48 h, evaporated to dryness and dissolved in 6M HCl and heated again for 24 h. After complete dissolution and subsequent evaporation, the residue was diluted in 2 mL of 2 M HNO_3. Sr, Rb and REE were separated using the Sr spec and Tru Spec resins (Pin et al., 1994). The Sr cuts were loaded onto Re filaments and analyzed by TIMS Triton Plus (Thermo electron) in static multicollection. The $^{87}Sr/^{86}Sr$ ratios were normalized to a $^{86}Sr/^{88}Sr$ ratio of 0.1194. Repeated analysis of the NBS 987 standard yielded an average of 0.710255 ± 0.000017.

3. Results

Our field prospection highlighted 118 new surface indicators of hydrothermal activity to the already 71 reported in previous studies (Aunay et al., 2013; Belle, 2014; Bénard et al., 2020; Frissant et al., 2003; Iundt et al., 1992; Lopoukhine and Stieltjes, 1978; Louvat and Allègre, 1997; Manès, n.d.; Marty et al., 1993; Poul, 1966; Rocher, 1988; Sanjuan et al., 2001). Their coordinates and description and the physiochemical parameters of the springs are given in Supplementary Material. We observed and measured 28 out of the 71 indicators from previous studies, and found that 9 more have since disappeared in landslides. Out of the total 189 field indicators, 28 are dry iron oxide/carbonate/sulfide dry deposits and 161 are thermal springs. Thermal springs temperatures range from 9.8 to 48°C, electrical conductivities range from 194 to 3370 µS/cm and pH range from 5.3 to 9.4. Mean values are 1050 ± 512 µS/cm for electrical conductivity, 6.9 ± 0.7 for pH and 20.8 ± 4.6°C for temperature. These wide ranges of physiochemical parameters reflect the variability of the contribution of the hydrothermal component to the geochemistry of the springs.

Major elements and Al, Sr, and Br concentrations were analyzed on 38 thermal springs (Table 1. For our study, we included analyses of thermal springs from previous studies (Aunay et al., 2013; Belle, 2014; Frissant et al., 2003; Iundt et al., 1992; Lopoukhine and Stieltjes, 1978; Louvat and Allègre, 1997; Sanjuan et al., 2001). For a comprehensive compilation of this literature data, see appendix A and B in Bénard et al., (2020). On a Piper diagram, most springs gather at the HCO_3 end in the anion triangle plot, and only a few springs tend toward the SO_4 or Cl ends (Figure 2). Therefore, most thermal springs

of Piton des Neiges can be considered bicarbonate waters. In the cation plot, some springs show a trend towards the Na+K pole in the cation plot but most plot in the middle.

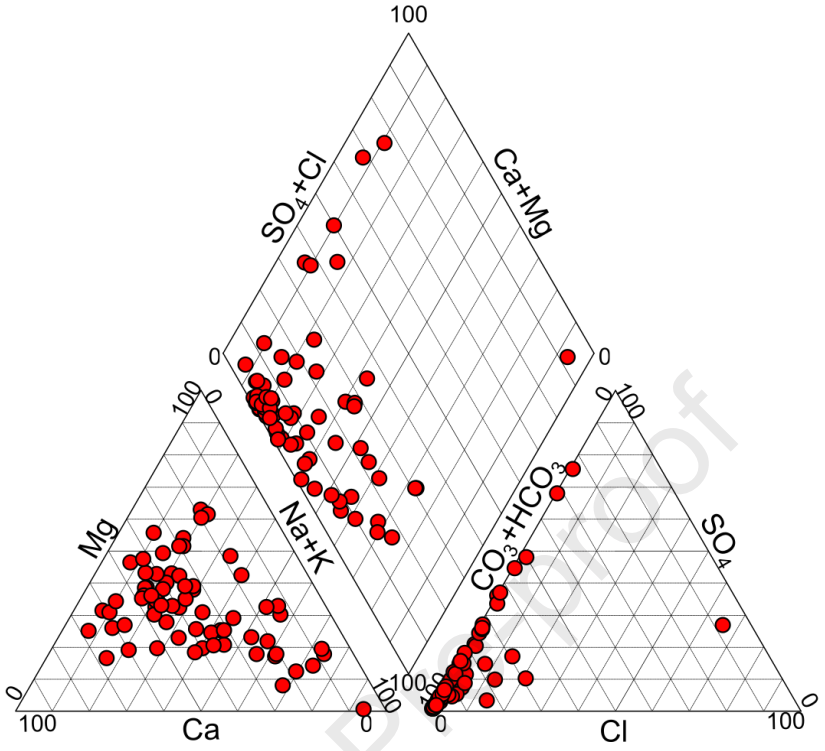

Figure 2: Piper diagram of thermal springs of Piton des Neiges. The composition of each thermal spring is the mean of all the available data from this study and the literature.

Springs for which several analyses are available over the years show very little variation of their geochemical composition. Their relative proportions of major elements display little variation over time (1 s.d. of Na + K, Ca + Mg, SO_4+Cl, HCO_3 mole fractions ≤ 8 %) with the exception of TR and OLIVbis.

The results of $\delta^{13}C$, $\delta^{18}O$ and δD analyses in thermal springs are presented in Table 1. $\delta^{13}C$ values range between -14.8 and 5.2 ‰. When considering the mean value of each spring, $\delta^{18}O$ and δD values for all thermal springs range from -8.58 to -5.4 ‰ and from -58.8 to -23.5 ‰, respectively. Additionally, surface water samples measured in rivers (Rivière Bras Rouge rBRO), Rivière du Mât (rRMA) and Ravine Blanche (rRBL) yielded $\delta^{18}O$ and δD values of -7.18 and -44.4 ‰, -7.97 and -51.3 ‰, and -7.26 and -46.1 ‰, respectively. These values are in the upper range of those measured in thermal springs.

Results of monthly monitoring of $\delta^{18}O$ and δD in rainwaters and thermal springs in the cirques of Salazie and Cilaos are presented in Table 2. Over the sampled period, the $\delta^{18}O$ and δD of the thermal springs TBA and IRN show almost no variation ($\delta^{18}O$=-6.81 ± 0.16 ‰ and δD=-40.2 ± 0.5 ‰ for TBA; $\delta^{18}O$=-8.08 ± 0.06 ‰ and δD=-51.2 ± 0.23 ‰ for IRN). In contrast, rainwaters exhibit a wide range of $\delta^{18}O$ and δD values, from -7.22 to -1.49 ‰ and -47.3 to +3.2 ‰ for Salazie, respectively, and from -9.68 to -1.31 ‰ and -66.3 to +4.4 ‰ for Cilaos, respectively.

Analyses of strontium isotopic ratios are presented in Table 1 for thermal springs and Table 3 for rocks. The $^{87}Sr/^{86}Sr$ ratios of Piton des Neiges thermal springs (0.704129 to 0.704364) are in the range of rocks values from Salazie and Cilaos (0.704041 to 0.704504, Table 3). Our new analyses of trachyte and syenite rocks display low $^{87}Sr/^{86}Sr$ ratios (0.704156 to 0.704215), in agreement with literature data available for these types of rocks (0.704153 to 0.704268, mean 0.704181, Nauret et al., 2019; Smietana, 2011).

315 Table 1: Physicochemical parameters, major elements concentrations, $\delta^{18}O$, δD, $\delta^{13}C$ and $^{87}Sr/^{86}Sr$ isotopic ratios in thermal springs of Piton des Neiges.

Spring	Location	Date dd/mm/yyyy	Electrical Conductivity (µS/cm)	pH	Temperature (°C)	Ca (mmol/L)	Mg (mmol/L)	Na (mmol/L)	K (mmol/L)	HCO_3 (mmol/L)	SO_4 (mmol/L)	Cl (mmol/L)	SiO_2 (mmol/L)	Br (µmol/L)	Al (µmol/L)	Sr (µmol/L)	$\delta^{18}O$ (‰ VMOW)	δD (‰ VMOW)	$^{87}Sr/^{86}Sr$	$\delta^{13}C$ (‰ PDB)
AGS*	Salazie	17/06/2015	1746	6.5	21.1	6.75	3.49	1.65	0.1	14.52	4.11	0.03	1.28		0.0					
BACH*	Salazie	15/06/2015	1260	6.9	25.6	2.85	2.58	3.94	0.12	14.38	0.14	0.07	1.33		0.1		-6.7	-41.6	0.704317	1.4
BB*	Cilaos	05/05/2017	1699	6.7	25.1	3.96**	3.29	5.89	0.11	15.48**	2.32	0.39	1.99	0.43	0.8	5.4	-8.06	-53.1	0.704139	-1.4
BB6	Cilaos	30/11/2017	1332	6.5	22.8	2.41	3.15	4.35	0.07	13.52	0.36	0.1	1.32	0.07	b.d.l.	2	-7.47	-49.7	0.704129	-2
BB7	Cilaos	30/11/2017	652	6.9	19.8	1.12	0.84	2.85	0.03	4.51	1.16	0.1	0.8	0.08	b.d.l.	0.8	-7.58	-50.6		-14.2
BBLEU1	Cilaos	29/06/2017	524	7.7	18.6	0.91	0.63	2.77	0.03	6.13	0.09	0.05	0.46	0.05	1.0	3.9	-8.08	-53.4	0.704203	-6.1
BC	St-Benoît	15/12/2015	3270	6.5	23	4.08	13.31	7.86	0.45	42.98		0.12	2.1	0.10	b.d.l.	1.3	-7.62	-43.4	0.704196	-3.2
BE	Cilaos	26/10/2017	1257		19.8	2.17	4.3	1.83	0.15		0.03	0.1	1.77	0.06	b.d.l.	5.9	-8.15	-55.1	0.704167	-1.3
BR14	Cilaos	06/03/2016	1630	6.2	42.4	2.22	2.38	10.68	0.32	19.52**		0.68	2.35	0.95	0.2	11	-8.19	-51.9	0.704156	-1.5
BR14	Cilaos	21/11/2015	1684	6.1	39.1	2.65	2.69	12.03	0.33	21.97**		1.07	2.39	0.57	0.1	13.1	-8.44	-52.5	0.704172	-0.2
BR14*	Cilaos	08/09/2017	1764	6.8	37.2	2.17**	2.54	12.36	0.35	19.10**	0.91	1.21	2.49	0.97	b.d.l.	12.6	-8.53	-53.7	0.704179	-0.8
BR16*	Cilaos	30/07/2016	2530	6.8	25.9	2.52**	2.39	18.35	0.86	24.93**		3.22	2.02	2.70	b.d.l.	8	-8.41	-52	0.704165	1.8
BR16*	Cilaos	29/10/2017	3370	6.5	29.1	2.70**	3.14	25.01	0.99	31.61**	0.48	5.13	2.58	4.02	b.d.l.	11.1	-8.67	-53.3	0.704162	0.6
BR21*	Cilaos	23/08/2016	1256	6.2	25.1	1.64**	0.58	9.8	0.1	12.98**	0.5	0.36	0.56	0.38	b.d.l.	17.6	-8.07	-51.7	0.704249	3
BR6	Cilaos	26/08/2017	1221	6.1	25.3	3.42	1.15	2.93	0.09	10.16	0.44	0.1	0.93	0.09	b.d.l.	10.9	-7.35	-46	0.704212	-1.5
BR9	Cilaos	20/03/2016	1149	6.0	26.5	2.53	3.06	2.6	0.12	13.85**		0.05	1.64	0.05	b.d.l.	10.5	-7.96	-53.1	0.704175	0.1
DUP*	Salazie	15/06/2015	714	8.1	23.3	1.39	1.25	2.78	0.08	7.23	0.39	0.06	0.96		b.d.l.		-6.5	-38.4	0.704224	3.4
EDN*	Salazie	16/05/2015	1855	6.4	25.5	3.17	6.17	3.99	0.22	23	0.12	0.05	2.34		0.0		-6.5	-38.7	0.704237	3
FSJ2	Salazie	14/07/2017	864	7.1	15.8	2	1.25	2.35	0.07	8.70**	0.07	0.08	1.36	0.08	b.d.l.	7.8	-5.96	-34.4	0.704240	-2.6
G3	Cilaos	20/03/2016	1416	6.2	22.4	3.34	4.27	2.66	0.13	17.97**		0.05	2	0.13	b.d.l.	18.1	-8.23	-51.9	0.704183	0.2
GDS*	Salazie	17/06/2015	1234	7.7	18.7	4.74	2.23	1.31	0.07	8.79	3.34	0.03	0.79	0.14	0.0		-5.9	-33.1	0.704330	1.7
IRN*	Cilaos	29/11/2017	2570	6.7		4.00**	4.19	15.13	0.19	29.48**	1.04	0.15	2.51	0.10	b.d.l.	19.8	-8.14	-51.1		
IRN*	Cilaos	05/05/2017	2510	6.5	35.1	**	4.16	15.01	0.21		1.01	0.17	2.32	0.11	b.d.l.	12.2	-8.05	-51		-1.2
IRN*	Cilaos	15/06/2017	2500	6.4	36	3.99**	4.08	14.79	0.2	28.98**	1.01	0.15	2.36	0.17	b.d.l.	19.7	-8.1	-51.2		-0.9
IRN*	Cilaos	26/10/2017	2570	6.4	34.3	4.05**	4.26	15.33	0.2	29.92**	1.04	0.15	2.43	0.11	b.d.l.	20	-8.06	-51		-0.5
IRN*	Cilaos	25/09/2017	2560	6.6	36.2	4.00**	4.15	15.05	0.2	29.36**	1.02	0.16	2.42	0.10	b.d.l.	19.4	-7.89	-50.9	0.704168	-0.5
IRN*	Cilaos	30/08/2017	2560	6.4	36.2	4.08**	4.17	15.46	0.22	28.97	1.04	0.21	2.41		b.d.l.	20	-8.04	-50.9		-0.4
MAN*	Salazie	16/06/2015	1395	6.6	30.6	3.3	2.69	4.39	0.2	16.57	0.11	0.07	1.76		0.0		-7.2	-43.4	0.704277	1.6
MAN	Salazie	19/08/2016	1520	6.7	30.4	3.6	2.84	4.45	0.21	17.16**	0.14	0.11	1.53	0.08	b.d.l.	9.7	-7.19	-42.5	0.704273	1.2
MANa	Salazie	19/08/2016	274	6.2	14.9	0.42	0.51	0.61	0.14	2.51**	0.03	0.05	0.65	0.04	b.d.l.	0.6	-8.58	-54.8	0.704240	1.5
MANc	Salazie	19/08/2016	687	5.9	17.5	1.27	1.5	1.79	0.24	7.39**	0.06	0.06	1.12	0.06	b.d.l.	2.6	-8.54	-53.8	0.704258	5.2
MANES	Cilaos	29/11/2017	2310	6.5	29.6	3.75	3.99	13.14	0.19	26.77**	0.9	0.26	2.21	0.12	b.d.l.	17.7	-8	-51.3		-0.9
MANES	Cilaos	26/10/2017	2340	6.0	30.3	3.55	3.99	13.02	0.2	23.82**	0.9	0.16		0.09		18.1	-8.06	-51.4		-1.4
MANES	Cilaos	25/09/2017	2310	6.6	30.8	3.78	3.99	13.18	0.2	27.00**	0.89	0.15		0.08		18.1	-7.98	-51		-1.3
MANES	Cilaos	30/08/2017	2320	6.4	30.7	3.72	3.93	12.94	0.2	26.52**	0.88	0.16		0.08		17.6	-8.02	-51.4		-0.8
MANES*	Cilaos	15/06/2017	2310	6.4	29.8	3.72**	3.86	13.02	0.2	26.52**	0.86	0.16		0.16		17.7	-8.04	-51.5		-1.2
MANES	Cilaos	05/05/2017	2300	6.4	30.5	3.66	3.99	13.23	0.19	26.75**	0.9	0.18				17.3	-8.03	-51.3		0
MVP1	Salazie	12/05/2017	476	7.9	21	1.56	0.88	0.48	0.04	2.69	1.29	0.11	0.59	0.22	0.8	4	-5.84	-35.2	0.704330	-12.9
OLIVbis	Salazie	22/11/2017	551	8.1	22.3		0.87	1.62	0.04	5.05**	0.45	0.11	0.5	0.08	b.d.l.		-6.01	-37.1	0.704364	-12.3
OLIVbis	Salazie	30/01/2018	735	7.8	22.3	1.92	1.23	1.59	0.04	2.39**	1.37	0.13			b.d.l.	7.1			0.704347	-12.1
PEND	Cilaos	29/11/2017	618	7.1	22.9	0.89	0.98	2.86	0.14	5.41**	0.6	0.13	0.94	0.11	b.d.l.	0.5	-8.18	-58.8	0.704212	-14.8

Spring	Location	Date dd/mm/yyyy	Electrical Conductivity (µS/cm)	pH	Temperature (°C)	Ca (mmol/L)	Mg (mmol/L)	Na (mmol/L)	K (mmol/L)	HCO_3 (mmol/L)	SO_4 (mmol/L)	Cl (mmol/L)	SiO_2 (mmol/L)	Br (µmol/L)	Al (µmol/L)	Sr (µmol/L)	$\delta^{18}O$ (‰ VMOW)	δD (‰ VMOW)	$^{87}Sr/^{86}Sr$	$\delta^{13}C$ (‰ PDB)
RB1*	Salazie	15/10/2016	929	6.0	19.8	2.30**	1.83	1.21	0.19	9.44**	0.08	0.05	1.62	0.09	b.d.l.	4.5	-6.5	-37.1	0.704308	-1.9
RB2	Salazie	15/10/2016	1030	6.1	19.8	3.11	1.94	1.25	0.15	11.26**	0.1	0.05	1.53	0.08	b.d.l.	6.7	-6.37	-36.6	0.704309	-1.9
RBGR1	Cilaos	30/06/2017	1334	6.6	19	1.78	4.17	2.86	0.03	14.1**	0.3	0.09	1.63	0.04	b.d.l.	0.6	-6.9	-45.9	0.704176	-4.3
RBR3	Cilaos	23/08/2016	379	7.5	12.1	0.96	0.74	0.83	0.06	3.9	0.27	0.02	0.52	0.02	b.d.l.	3.6	-8.01	-50.4	0.704181	2.8
RBR5	Cilaos	23/08/2016	634	7.8	14	1.8	1.34	1.21	0.06	4.16	1.69	0.05	0.44	0.02	b.d.l.	11.6	-7.76	-48.1	0.704185	-0.2
RBR8	Cilaos	23/08/2016	1145	7.4	13.5	4.72	1.76	0.97	0.06	4.61	4.94	0.07	0.28	0.02	b.d.l.	21.9	-7.97	-50.2	0.704169	0.9
RM22	Salazie	17/05/2017	660	7.4	23.3	1.32	2.14	0.64	0.1	6.74	0.45	0.08	1.24	0.09	0.5	3	-5.98	-36.5	0.704216	-7.5
RR1*	Cilaos	30/07/2016	1586	6.2	32.5	2.29**	1.41	10.3	0.3	14.72**	0.91	1.47	1.77	1.25	b.d.l.	9.2	-8.48	-56.3	0.704167	2.6
TB*	Salazie	22/11/2017	1410	6.3	34.4	2.14**	1.03	9.35	0.29	14.08**	0.57	0.75	1.09	0.63	b.d.l.	7.6	-6.42	-38.7	0.704194	-1.7
TBA*	Salazie	15/06/2015	1718	6.3	26.6	4	2.46	7.07	0.16	16.95	0.97	0.1	2.08		0.0					
TBA	Salazie	11/05/2017	1651	7.0	26.4		2.5	6.96	0.16	14.74	1.85	0.11	2.07		b.d.l.		-6.59	-39.9	0.704265	0.3
TR*	Salazie	21/07/2017	379	7.3	20.8	0.71**	0.78	0.73	0.04	1.51**	1.08	0.07	0.54	0.11	0.9	1.9	-6.69	-41.1	0.704333	-8
TR*	Salazie	30/01/2018	1016	7.5	20.8		2.71	1.05	0.06		5.07	0.09	0.6		1.2				0.704308	-6.4
VERO	Cilaos	29/11/2017	1980	6.2	29.7	3.2	3.37	10.69	0.16	22.39**	0.74	0.14	2.03	0.10	b.d.l.	15.6	-7.97	-51.3		-2
VERO	Cilaos	26/10/2017	1994	6.1	29.5	3.13	3.47	10.93	0.16	21.74	0.74	0.12		0.10		15.4	-8	-51.5		-2.1
VERO	Cilaos	25/09/2017	1988	6.4	29.9	3.16	3.4	10.69	0.25	22.38**	0.72	0.25				15.3	-7.96	-51.4		-2.2
VERO*	Cilaos	15/06/2017	1938	6.2	29.5	3.16**	3.33	10.56	0.16	20.79	0.68	0.14		0.04		15.3	-7.96	-51.6		-2.2
VERO*	Cilaos	30/08/2017	1986	6.2	29.7	3.12**	3.36	10.65	0.16	22.21**	0.72	0.13		0.06		15.2	-7.96	-51.2		-2.2
VERO	Cilaos	05/05/2017	1888	6.4	29.3	3.01	3.16	10.21	0.18	19.52	0.67	0.14		0.05		14.7	-7.93	-51.3		-2.3

316 *Bénard et al., (2020) *; **corrected values (re-analyzed Ca concentrations and HCO_3 concentrations estimated from ionic balance)*

Table 2: monitoring of $\delta^{18}O$ and δD values (‰ VSMOW) from rainwaters and thermal springs (TBA and IRN) in the cirques of Salazie and Cilaos. Rainwater samples correspond to a cumulate of rainfalls collected over about 4 weeks. Spring samples were taken when rainwaters were collected. Rainfall amount (mm) is deduced from the collected rain volume, except when information is missing (no data or overflow indicated by an *). In the latter case, we used the rainfall data from the closest METEOFRANCE meteorological station accessible at their online data repository publitheque.meteo.fr (we accounted for a proportionality coefficient to adjust for the systematic difference between METEOFRANCE and our rainfall data).

Location	Sampling period (Rain)/ Sampling date (Spring, end of period) Dates in dd/mm/yy	Rain				Spring (TBA in Salazie, IRN in Cilaos)	
		$\delta^{18}O$ (‰)	δD (‰)	Volume (L)	Rainfall (mm) corrected	$\delta^{18}O$ (‰)	δD (‰)
Salazie	07/04/17-11/05/17	-4.06	-16.8	5.2	67.5	-6.59	-39.9
	11/05/17-14/06/17	-3.11	-9.8	1.6	20.0	-6.72	-40.4
	14/06/17-21/07/17	-2.70	-5.2	0.7	9.0	-6.79	-40.3
	21/07/17-25/08/17	-2.07	1.8	1.2	14.9	-6.83	-40.0
	25/08/17-21/09/17	-3.77	-15.7	0.9	11.0	-6.92	-41.1
	21/09/17-19/10/17	-1.86	1.5	1.0	13.4	-6.97	-40.7
	19/10/17-22/11/17	-2.89	-8.7	2.6	34.1	-6.97	-40.8
	22/11/17-20/12/17	-1.49	3.2	0.0*	8.6	-7.05	-40.5
	20/12/17-30/01/18	-7.22	-47.3	20.0*	298.4	-6.53	-39.0
	30/01/18-31/05/18	-6.90	-42.8	20.0*	506.2	-6.60	-39.7
	31/05/18-17/07/18	-2.47	-1.3	2.0	25.8	-6.74	-39.6
	17/07/18-18/10/18	-2.24	-1.8	2.9	36.8	-6.88	-40.5
	18/10/18-07/11/18	-2.58	-10.0	1.4	18.1	-6.96	-40.1
	08/11/18-21/01/19	-5.61	-32.3	11.1	143.3	-6.81	-40.3
	21/01/19-12/02/19	-5.19	-29.0	1.6	20.7	-6.83	-40.5
	12/02/19-13/03/19	-3.61	-15.5	1.9	23.9	-6.89	-40.3
	13/03/19-17/04/19	-4.73	-25.3	2.4	31.0	-6.96	-40.4
	17/04/19-28/05/19	-2.66	-4.4	1.5	19.4	-7.03	-40.5
Cilaos	30/03/17-05/05/17	-4.40	-18.4	0.0*	53.7	-8.05	-51.0
	05/05/17-15/06/17	-3.61	-18.2	1.0	12.3	-8.10	-51.2
	15/06/17-28/07/17	-2.67	-4.6	0.7	9.0	-8.09	-51.2
	28/07/17-30/08/17	-2.70	-5.1	1.0	12.9	-8.04	-50.9
	30/08/17-25/09/17	-2.76	-2.8	0.8	9.7	-7.89	-50.9
	25/09/17-26/10/17	-1.31	4.4	0.3	3.2	-8.06	-51.0
	26/10/17-29/11/17	-3.16	-11.7	1.8	23.6	-8.14	-51.1
	29/11/17-21/12/17	-2.74	-7.2	0*	10.1	-8.09	-51.3
	21/12/17-06/02/18	-8.34	-57.8	20.0*	304.4	-8.05	-51.5
	06/02/18-21/05/18	-9.68	-66.3	20.0*	430.9	-8.10	-51.6
	21/05/18-15/10/18	-2.25	-1.9	2.6	32.9	-8.10	-50.9
	15/10/18-08/11/18	-4.97	-25.3	2.2	27.8	-8.11	-51.1
	08/11/18-05/12/18	-3.70	-17.3	2.0	25.2	-8.13	-51.4
	05/12/18-22/01/19	-5.69	-34.8	3.9	50.4	-8.12	-51.6
	22/01/19-13/02/19	-5.20	-25.8	2.0	25.8	-8.11	-51.2
	13/02/19-14/03/19	-3.59	-15.8	0.9	11.6	-8.11	-51.2
	14/03/19-18/04/19	-4.86	-26.6	1.6	20.7	-8.12	-50.8
	18/04/19-29/05/19	-3.24	-8.3	0.6	7.1	-8.17	-50.9

Table 3: $^{87}Sr/^{86}Sr$ isotopic ratios of rocks from the cirques of Salazie and Cilaos.

Sample	Rock type	Source of data	Location	X (RGR92 /UTM40S)	Y (RGR92 /UTM40S)	Sr (ppm)	$^{87}Sr/^{86}Sr$	Error (2σ)	Stage
BR14	Syenite	This study	Cilaos			40.0	0.704184	0.000006	Differentiated
CHAP	Syenite		Cilaos			149	0.704215	0.000023	Differentiated
RN18-5	Syenite		Salazie			634	0.704182	0.000015	Differentiated
BAF1-6	Trachyte		Summit			498	0.704156	0.000010	Differentiated
PdNMS21	Aphyric Basalt	Smietana, 2011	Cilaos	340237	7648804	393.8	0.704153	0.000004	Shield
PdNMS21	Aphyric Basalt		Cilaos	340237	7648804	289.2	0.704153	0.000004	Shield
CB16290513	Gabbro	Berthod, 2016	Salazie	343698	7670796		0.704220	0.000010	Shield
CB2150914	Gabbro		Salazie	343808	7669712	54.8	0.704166	0.000009	Shield
CB2260513	Gabbro		Salazie	344106	7670815	288.4	0.704258	0.000007	Shield
CB3230914	Syenite		Salazie	343534	7670756	331.6	0.704190	0.000008	Differentiated
CB3A260513	Gabbro		Salazie	344120	7670828	245.7	0.704255	0.000010	Shield
SAB 1	Syenite	Nauret et al., 2019	Salazie	341515	7669423	245.0	0.704155	0.000008	Differentiated
SAL 1	Basalt		Salazie	344105	7670824	542.6	0.704283	0.000022	Shield
SAL 102	Oceanite		Salazie	344238	7670893	497.5	0.704041	0.000008	Shield
SAL 106	Gabbro		Salazie	344194	7670885	558.5	0.704290	0.000008	Shield
SAL 110	Gabbro		Salazie	343667	7670778	472.5	0.704256	0.000008	Shield
SAL 153	Oceanite		Salazie	342913	7674274	228.9	0.704085	0.000007	Shield
SAL 18	Gabbro		Salazie	344180	7670872	512.7	0.704290	0.000012	Shield
SAL 200	Trachy-Basalt		Salazie	343775	7669845	573.9	0.704158	0.000007	Differentiated
SAL 200 (duplicate)	Trachy-Basalt		Salazie	343775	7669845		0.704159	0.000007	Differentiated
SAL 201	Trachy-Basalt		Salazie	343895	7669717	376.8	0.704268	0.000006	Differentiated
SAL 203	Trachy-Basalt		Salazie	343317	7670409	487.4	0.704167	0.000007	Differentiated
SAL 206	Dunite		Salazie	344492	7668744	23.9	0.704277	0.000011	Shield
SAL 48	Basalt		Salazie	343567	7670290	512.4	0.704223	0.000008	Shield
SAL 51	Basalt		Salazie	343482	7670368	357.1	0.704223	0.000010	Shield
SAL 88	Trachyte		Salazie	344734	7670476	531.1	0.704169	0.000008	Differentiated
SAL 88 (duplicate)	Trachyte		Salazie	344734	7670476		0.704185	0.000009	Differentiated
RUN 027-2006	Olivine basalt		Cilaos			89.0	0.704154	0.000008	Shield
RUN 029-2006	Olivine basalt		Cilaos			73.5	0.704144	0.000010	Shield
RUN 040-2006	Benmoreite		Salazie			89.0	0.704504	0.000015	Differentiated
ANTN	Benmoreite		Summit			176	0.704176	0.000014	Differentiated
RN18-9	Trachyte		Summit			256	0.704153	0.000010	Differentiated

4. Discussion

4.1. Spatial distribution of hydrothermal features

In this section, we study the spatial distribution of several geochemical features related to hydrothermal activity: the occurrence of field indicators of hydrothermal activity, the temperature and electrical conductivity at the outlets of springs and their CO_2 partial pressure. This spatial distribution is then superimposed to the main geological features to decipher if they may constitute heat sources or drains for the thermal fluids.

4.1.1. Field indicators of hydrothermal activity

Thermal springs and dry deposits of iron oxide/carbonate/sulfide, which are indicators of hydrothermal activity, are observed in the three cirques (Figure 3) with two springs reaching farther east in Saint-Benoît. The majority of them are found in the cirques of Salazie and Cilaos, with a greater

abundance in the upper slopes of the cirques beneath the summit of Piton des Neiges. A first important result of our field prospection is that hydrothermal indicators largely extend outside the proposed caldera, suggesting that the hydrothermal system is not directly fed by this major volcanic structure nor limited by it. Secondly, most of these indicators are spread along a ~N25° axis, coinciding with the N30° rift zone defined by Chaput et al., (2017, 2014). This N25° spatial repartition is not biased by prospecting, as rivers from the northeastern part of Salazie, from the western part of Cilaos, from Mafate, from the two branches of the Grand Bassin depression, and from the Marsouins basin were surveyed and found to be devoid of thermal springs. Based on a study of outcropping planar intrusions, Chaput et al., (2017) showed that the N30°E rift zone is composed of mafic and differentiated dykes, implying a more recent activity than the N110-160° rift zone composed only of mafic intrusions. Our study confirms that the N30° rift zone is the most recently active volcano-tectonic lineament in the edifice, sufficiently young to provide heat for a shallow hydrothermal system. Thirdly, dry deposits (sulfides, oxides or carbonates) are mostly found at the external parts of the area containing hydrothermal indicators, and principally at the northern and southern extremities of this ~N25°-elongated zone. This suggests that dry hydrothermal indicators correspond to the external limits of the hydrothermal system. Interestingly, the two boreholes drilled in Salazie are located in this zone of dry hydrothermal indicators, possibly outside the hydrothermal system, which may explain why these two boreholes found heat but no water yield.

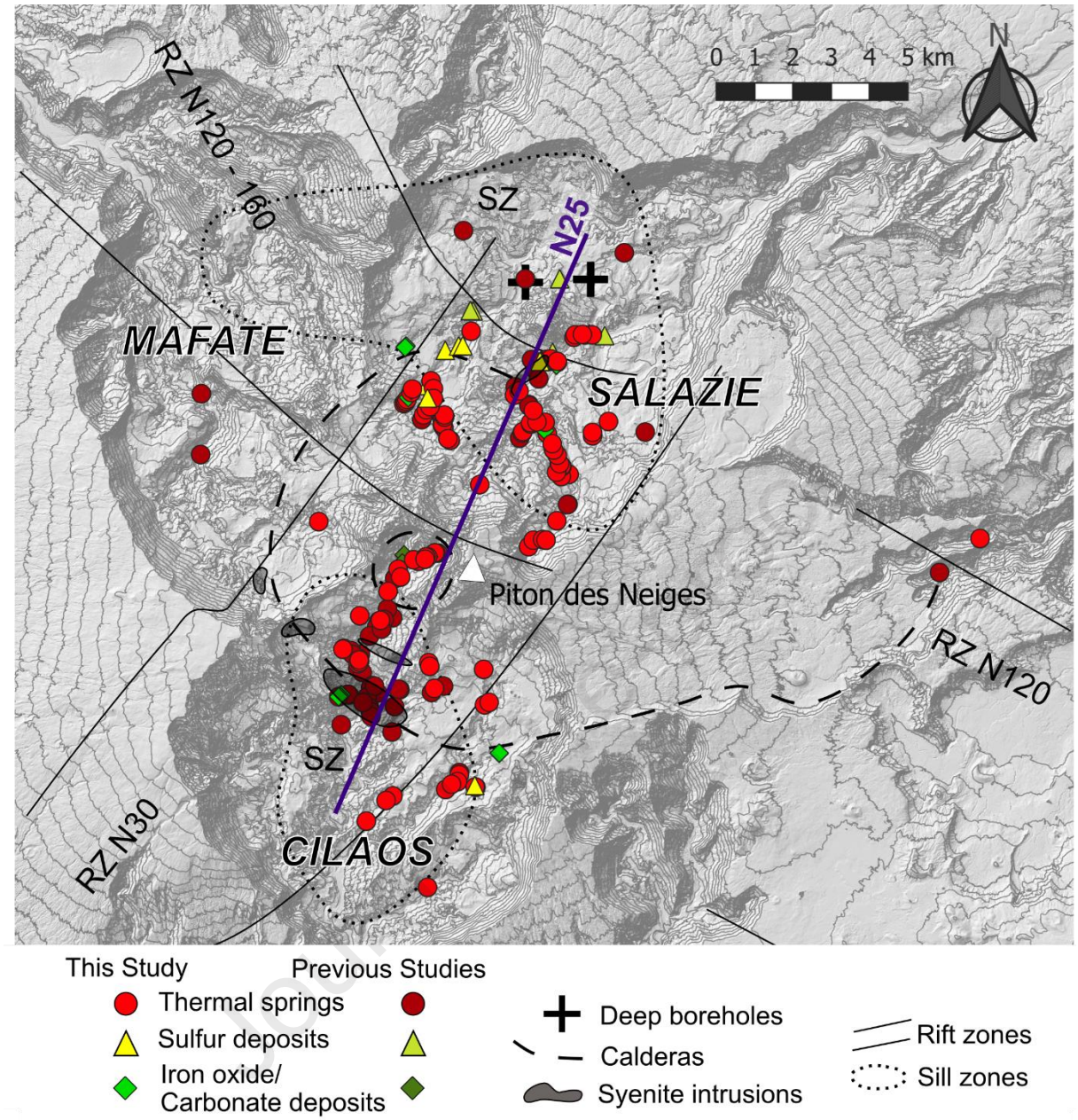

355

356 Figure 3: Map of the field indicators of hydrothermal activity at Piton des Neiges volcano from this study (bright
357 shades) and previous studies (darker shades, Aunay et al., 2013; Belle, 2014; Frissant et al., 2003; Iundt et al.,
358 1992; Lopoukhine and Stieltjes, 1978; Louvat and Allègre, 1997; Sanjuan et al., 2001). These indicators include
359 thermal springs and sulfur, iron oxide, or carbonate dry deposits. Most of the indicators are spread along a ~N25°
360 axis, coinciding with the N30° rift zone.

361 *4.1.2. Temperature and electrical conductivity*

362 High temperatures and elevated amounts of total dissolved solids (proxied by EC) at the outlet of
363 thermal springs are indicators of hydrothermal activity. These physicochemical parameters can be
364 modified during fluid upflow from the geothermal reservoir to the surface by mixing with shallow cold
365 waters, by further interaction with the surrounding rocks, or by cooling and deposition of secondary
366 minerals. Thermal springs display various degrees of enrichment in dissolved solids and warming
367 compared to rivers and groundwaters of Salazie and Cilaos (Figure 4), reflecting varying contributions
368 of a hydrothermal component. Those displaying higher values for outlet temperature and/or EC
369 indicate a closer reservoir, a faster transfer from the reservoir to the surface, a higher intensity of

water/rock interaction, or a lower dilution by cold waters. These physicochemical parameters are thus of paramount importance in geothermal exploration to locate zones of fastest circulation and/or of highest fluid temperature. The thermal springs of Piton des Neiges are represented according to their outlet temperature and EC in Figure 5. This figure shows that the hottest and most mineralized springs are not only located along the N30°E rift zone, but also in immediate vicinity of syenite intrusions and/or along the proposed rim of the caldera. Previous work suggested that syenite intrusions, thought to delineate the caldera, play at least a role of drain transferring thermal waters from the reservoir to the surface, and possibly even constitute the heat source and/or the reservoir itself (e.g. Frissant et al., 2003; Sanjuan et al., 2001). Our study strengthens these conclusions, as they remain valid even with our larger dataset.

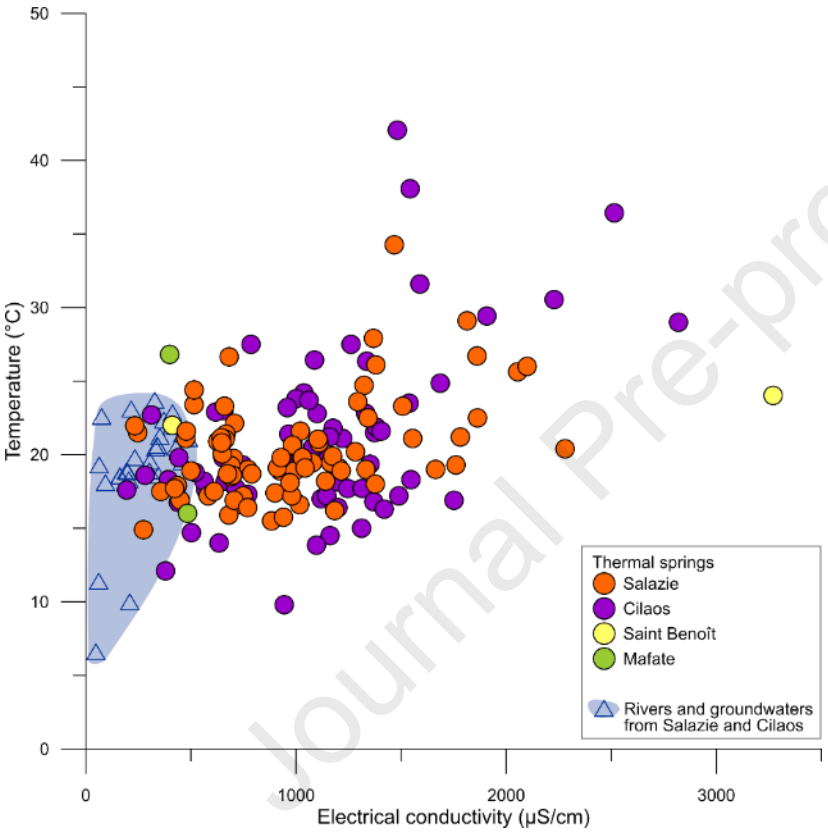

Figure 4: Mean temperature (°C) and electrical conductivities (µS/cm) of thermal springs from Piton de Neiges (this study, Aunay et al., 2013; Belle, 2014; Frissant et al., 2003; Iundt et al., 1992; Lopoukhine and Stieltjes, 1978;

Louvat and Allègre, 1997; Marty et al., 1993; Poul, 1966; Sanjuan et al., 2001) and rivers and groundwaters of Salazie and Cilaos (this study, Belle, 2014; Louvat and Allègre, 1997).

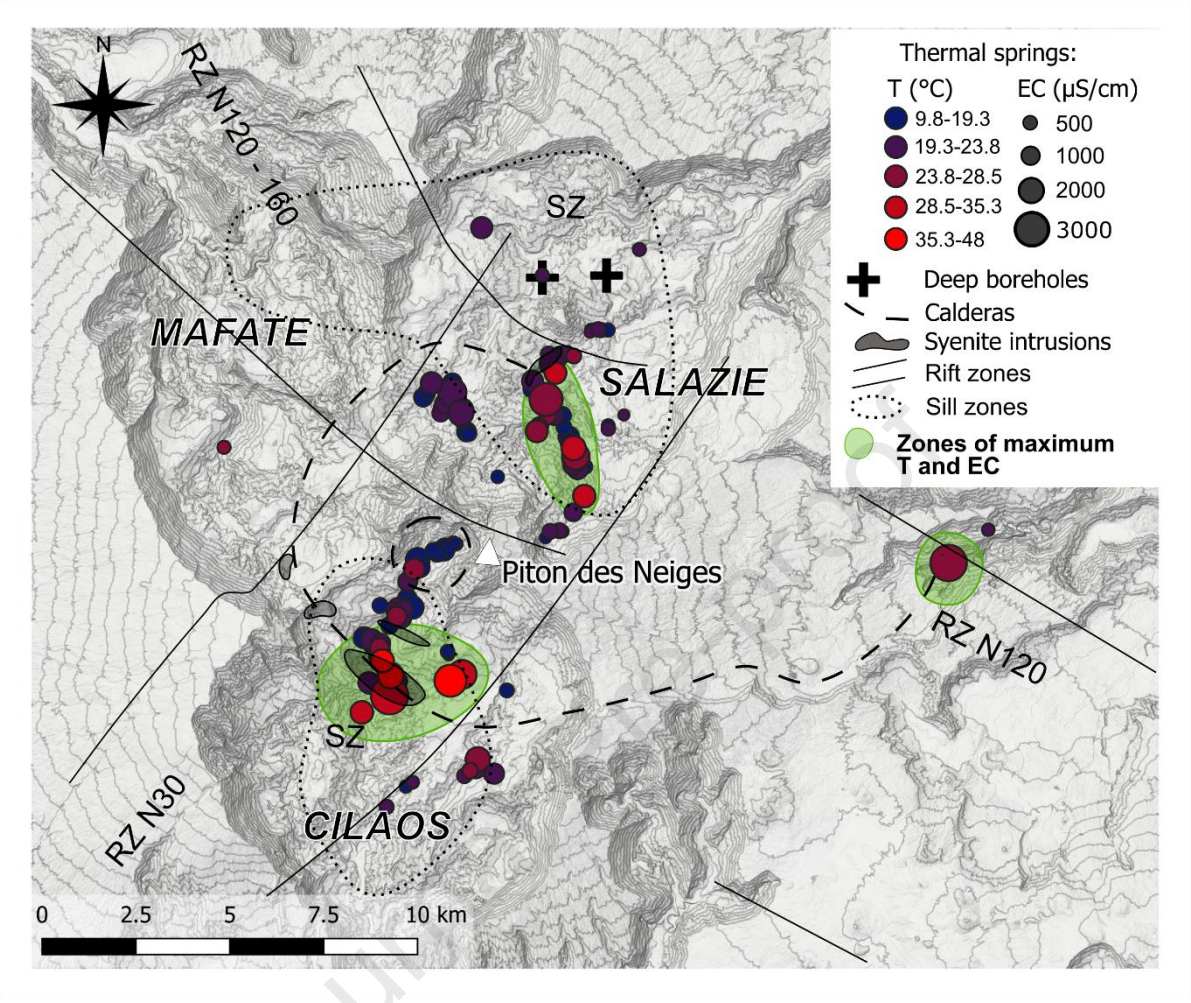

Figure 5: Spatial distribution of temperature (represented by a color scale) and electrical conductivity (EC in µS/cm, represented by symbol size) in the thermal springs of Piton des Neiges. Green fields represent zones of highest temperatures and EC, and hence of most promising geothermal resource according to these parameters. Volcano-tectonic structures (rift zones, sill zones, syenite intrusions, and calderas) are also represented.

4.1.3. Magmatic CO_2

All the thermal springs of Piton des Neiges analyzed in previous studies display evidence of interaction with magmatic CO_2, which essentially comes from mantle degassing associated with the Réunion hotspot (Bénard et al., 2020). The $\delta^{13}C$ signature of this mantellic CO_2 has been estimated from gas and fumarole samples of Piton de la Fournaise, the active volcano of La Réunion, and is comprised between -0.5 and -8 ‰ (Boudoire et al., 2018; Marty et al., 1993; Trull et al., 1993). Bénard et al., (2020) showed that higher values may be measured in thermal springs due to loss of gaseous CO_2 from waters which results in isotopic fractionation. Lower values may also be expected due to mixing with a biogenic carbon source with $\delta^{13}C \leq -20$ ‰ (Liuzzo et al., 2015). The newly measured values of $\delta^{13}C$ in thermal springs (from -14.8 to 5.15 ‰) from this study are consistent with the previous observations. Only four springs (BB7, MVP1, OLIVbis, PEND) display $\delta^{13}C$ values lower than -8 ‰, indicating a slight biogenic contribution. Therefore, magma degassing is the main carbon source in thermal springs and consequently, CO_2 can be used to highlight magmatic processes.

Consequently, we use the spatial distribution of the carbon content to locate zones of maximum CO_2 degassing, which may be interpreted as preferential pathways in the edifice for the rise of deep fluids. For each thermal spring, we computed the mean partial pressure of CO_2 (PCO_2, Table 4) at the outlet, from the water compositions displayed in Table 1 and using the "Diagrammes" software (created by R. Simler, Université d'Avignon et pays du Vaucluse, http://www.lha.univ-avignon.fr/LHA-Logiciels.htm) from PhreeqC, USGS®, with the WATEQ4F thermodynamic database (Ball and Nordstrom, 1991). Most of the gas being already lost at the spring outlet (Bénard et al., 2020; Marty et al., 1993; Sanjuan et al., 2001), PCO_2 cannot be considered as entirely representative of the total carbonate species' concentrations at depth. However, the preservation of a high PCO_2 in thermal springs is an indicator of an initial elevated CO_2 input and/or a shorter pathway from depth to surface. In Figure 6, we displayed the spatial distribution of PCO_2 along with geological features. It is worth noting that the thermal springs with the highest PCO_2 are not necessarily those with a high outlet temperature or EC, showing that CO_2 input is disconnected from the heat source. Nevertheless, as for temperature and EC, the most enriched springs (PCO_2 > 500 mbar) are those located in the N30°E rift zone and in the vicinity of syenite intrusions and/or along the proposed rim of the caldera, except for spring BC. The thermal spring BC, also displaying a high PCO_2, is located west of these structures, on the rift zone N120°E running throughout the island between Piton de la Fournaise and Piton des Neiges. CO_2 anomalies in soils have been observed along this rift zone (Boudoire et al., 2017). This spatial repartition suggests that the N30°E and N120°E rift zones and syenite intrusions and the larger caldera represent preferential pathways for the rise of CO_2 into the hydrothermal system.

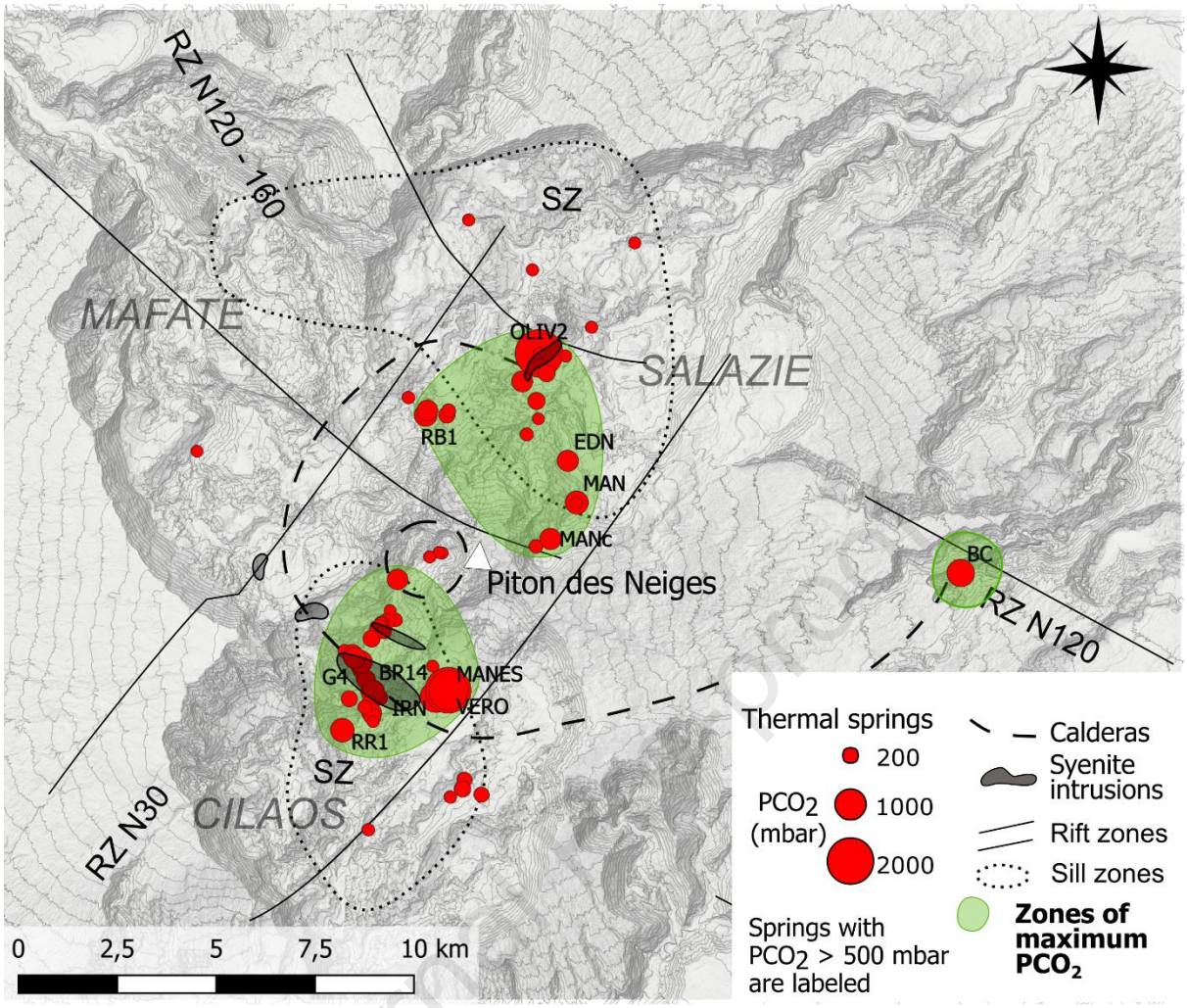

423

424 Figure 6: Spatial distribution of the mean partial pressure of CO_2 (PCO_2, in mbar) at the outlet of thermal springs
425 from Piton des Neiges, relative to volcano-tectonic structures (rift zones, sill zones, syenite intrusions, calderas).
426 Green fields represent zones of higher PCO_2, which are interpreted as zones of preferential mantle degassing.
427 Volcano-tectonic structures (rift zones, sill zones, syenite intrusions, and calderas) are also represented.

428 ## 4.2. Hydrogeological features

429 ### *4.2.1. Contamination by elements originating from seawater*

430 From the study of the $\delta^{37}Cl$ signature of thermal springs, Bénard et al., (2020) showed that two main
431 end-members contribute to their Cl budget: seawater and freshwater recharge. This is confirmed by
432 the Cl/Br concentration ratios obtained from this study which correspond to that of seawater (Figure
433 7). This seawater contamination likely does not originate from a current connection to the sea, as
434 saltwater intrusion is limited to coastal areas in La Réunion (Dumont et al., 2018). It could however
435 come from a trapped ancient reservoir or from seawater residual brines from when the area was still
436 connected to the sea, as observed in other volcanic islands (Herrera and Custodio, 2014). Whatever its
437 origin, this seawater Cl source is located at a depth of at least that of the seawater table.

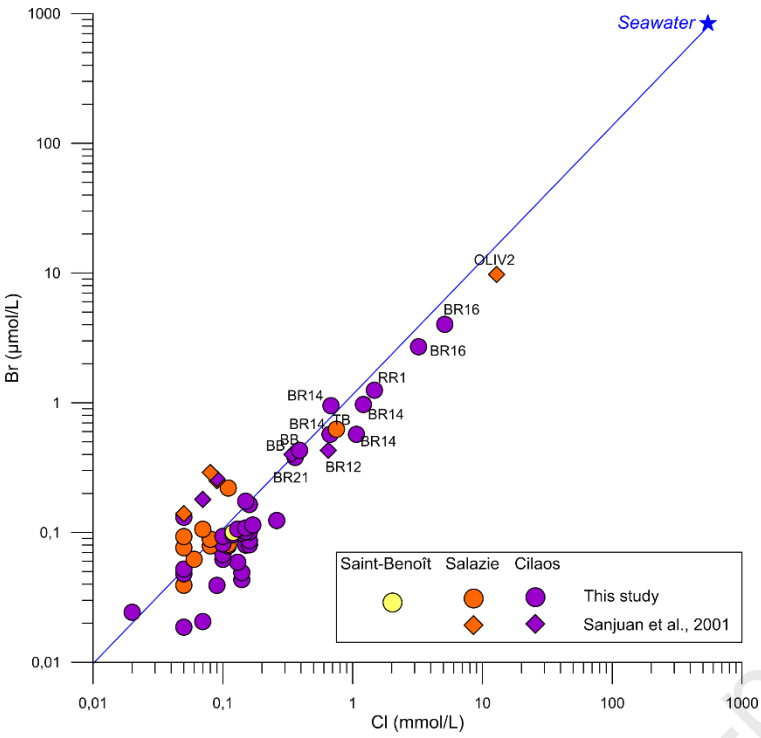

438

439 Figure 7: Cl and Br molar concentrations of the thermal springs of Piton des Neiges (This study, Sanjuan et al.,
440 2001) compared to the seawater dilution line.

441 In this section, we quantify the contamination by seawater Cl in thermal springs and use its spatial
442 distribution to locate the seawater Cl source in connection with the hydrothermal system. For each
443 thermal spring, we calculated the molar proportion of seawater contamination in thermal springs (f_{sea},
444 in mol%) using Cl as a conservative tracer, as shown in equation 1 (Appelo and Postma, 2005):

445 $$f_{sea} = \frac{m_{sample} - m_{fresh}}{m_{sea} - m_{fresh}} \quad (1)$$

446 where m_{sample}, m_{sea}, and m_{fresh} represent the Cl molar concentrations of the sampled thermal spring, of
447 seawater and of freshwater recharge, respectively. For each spring, m_{sample} is calculated as the median
448 composition of all available Cl analyses from this study and previous studies. We use the mean Cl
449 concentration of seawater for m_{sea}. For freshwater recharge, we considered a representative set of
450 131 analyses of groundwaters and river waters from Réunion Island (Aunay et al., 2012; Aunay and
451 Gourcy, 2007; Belle, 2014; Frissant et al., 2005; Louvat and Allègre, 1997; Petit et al., 2013) as
452 background values. We used the median Cl concentration of this dataset for m_{fresh}. There is very little
453 seawater contamination in the thermal springs of Piton des Neiges. Out of the 70 thermal springs for
454 which Cl concentrations are available, 61 contain less than 0.1 mol% seawater (Table 4). The highest
455 proportion of seawater is found in OLIV2 spring, reaching 2.34 mol%. The hydrothermal system is thus
456 located above the top of the seawater table, except for a limited number of springs whose drain may
457 root deep enough to intersect a seawater, Cl-rich reservoir. Seawater Cl contamination is found in the
458 vicinity of syenite intrusions and along the rim of the caldera, as are the hottest and most mineralized
459 thermal springs (Figure 8). This suggests that these structures represent pathways for the deepest
460 geothermal fluids reaching the surface.

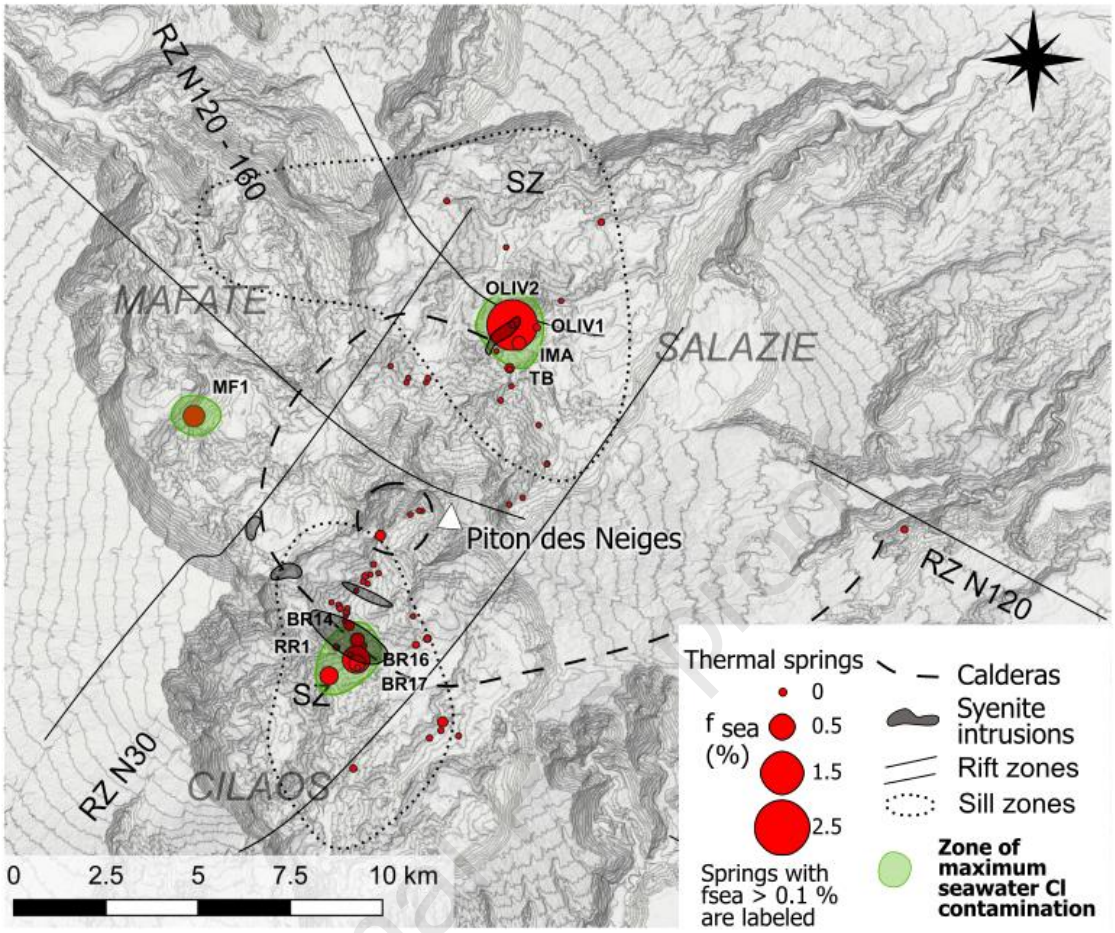

461

462 Figure 8: Spatial distribution of seawater contamination (in mol%) in the thermal springs of Piton des Neiges relative
463 to volcano-tectonic structures (rift zones, sill zones, syenite intrusions, and calderas). Green fields represent zones
464 of highest seawater contamination, interpreted as the deepest drains for the ascent of hydrothermal fluids. Volcano-
465 tectonic structures (rift zones, sill zones, syenite intrusions, and calderas) are also represented.

466

Table 4: Mean values of partial pressure of CO_2 at spring outlet (PCO_2, in mbar), molar proportion of seawater contamination (f_{sea}, in mol%), $\delta^{18}O$ and δD (in ‰ VSMOW) for each thermal spring.

Thermal spring	Mean PCO_2 (mbar)	Mean f_{sea} (mol%)	Mean $\delta^{18}O$ (‰)	Mean δD (‰)	Thermal spring	Mean PCO_2 (mbar)	Mean f_{sea} (mol%)	Mean $\delta^{18}O$ (‰)	Mean δD (‰)
AGS	237	0.00			G2	101	0.00		
BACH	70	0.00	-6.70	-39.4	G3	381	0.00	-8.23	-51.9
BB	162	0.05	-8.13	-53.7	G4	537	0.00		
BB6	249	0.00	-7.47	-49.7	GDS	95	0.18	-5.40	-28.3
BB7	33	0.00	-7.58	-50.6	IMA	259	0.01		
BBLEU1	7	0.00	-8.08	-53.4	IRN	1075	0.00	-8.07	-51.1
BC	865	0.01	-7.62	-43.4	MAN	628	0.00	-7.24	-43.6
BE	213	0.00	-8.15	-55.1	MAN G	12	0.00	-7.00	-39.8
BR1	97	0.00			MANa	90	0.00	-8.58	-54.8
BR10	387	0.00			MANc	530	0.01	-8.54	-53.8
BR11	16	0.00			MANES	1900	0.39	-8.04	-51.7
BR12	382	0.04	-8.20	-50.5	MF1	0	0.00		
BR13	6	0.00			MVP1	2	0.23	-5.84	-35.2
BR14	641	0.13	-8.33	-52.5	OLIV1	28	2.34	-6.50	-40.1
BR15	72	0.01			OLIV2	2583	0.00	-7.80	-45.9
BR16	440	0.68	-8.54	-52.7	OLIVbis	4	0.00	-6.01	-37.1
BR17	273	0.21			PC	17	0.01		
BR18	3	0.00			PEND	23	0.00	-8.18	-58.8
BR2	4	0.00			PISSA	154	0.00	-6.70	-41.4
BR21	487	0.05	-8.07	-51.7	RB1	588	0.00	-6.50	-37.1
BR27	265	0.01			RB2	484	0.00	-6.37	-36.6
BR3	220	0.00			RBGR1	174	0.00	-6.90	-45.9
BR4	120	0.00			RBR3	6	0.00	-8.01	-50.4
BR5	66	0.01			RBR5	4	0.00	-7.76	-48.1
BR6	404	0.00	-7.35	-46.0	RBR8	8	0.00	-7.97	-50.2
BR7	279	0.00			RFOUQ	496	0.00	-6.50	-37.9
BR8	67	0.00			RM22	16	0.25	-5.98	-36.5
BR9	603	0.00	-7.96	-53.1	RR1	656	0.01	-8.48	-56.3
DUP	3	0.00	-6.50	-38.4	sRMAT	14	0.00	-5.90	-36.5
EDN	517	0.00	-6.50	-38.7	sRMAT2	46	0.04	-6.20	-35.5
FJ1	93	0.00			sRMAT3	43	0.12		
FJ2	224	0.00			TB	305	0.00	-6.42	-38.7
FJ3	106	0.00			TBA	291	0.00	-6.83	-40.5
FSJ2	35	0.00	-5.96	-34.4	TR	7	0.01	-6.50	-40.7
G1	108	0.00			VERO	1530		-7.98	-51.4

4.2.2. Recharge

Mean values of $\delta^{18}O$ and δD for each thermal spring computed from our new and previous data (Table 4) plot close to the local meteoric water line (Figure 9.A). This $\delta^{18}O$ and δD signature indicates that the hydrothermal system is supplied by rain infiltration, as already evidenced by Bénard et al., (2020). With our new data, however, $\delta^{18}O$ and δD reveal a dichotomy between the thermal springs of Salazie and Cilaos. $\delta^{18}O$ and δD are less negative in the cirque of Salazie (from -7.80 to -4.9 ‰ and from -45.9 to -23.5 ‰, respectively) than in Cilaos (from -8.67 to -6.70 ‰ and from -58.8 to -41.4 ‰, respectively), except for the two springs at the extreme south of the cirque of Salazie MANa (-8.6 and -54.8 ‰) and MANc (-8.5 and -53.8 ‰, respectively) that show very negative values compatible with the Cilaos group.

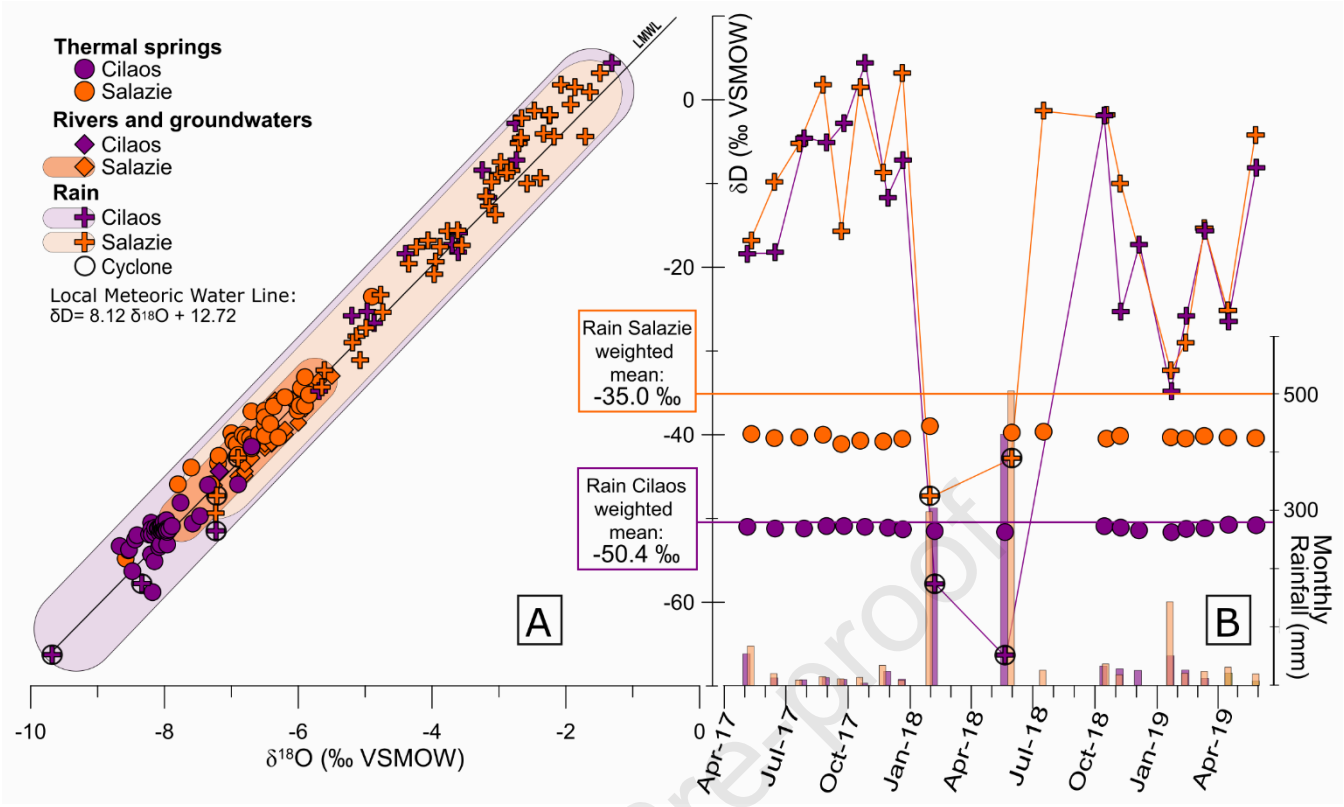

Figure 9: A. Mean $\delta^{18}O$ and δD isotopic ratios of thermal springs (this study, Aunay et al., 2013; Belle, 2014; Sanjuan et al., 2001) compared to that of river waters, groundwaters (this study, Belle, 2014; Louvat and Allègre, 1997) and rainwaters (this study, Belle, 2014; Grunberger, 1989; IAEA/WMO, 2019) from Salazie and Cilaos. Rainwaters from cyclones are circled in black. B. Comparative monitoring of the δD isotopic ratios (‰ VSMOW) of thermal springs and rain in Salazie and Cilaos, relative to rainfall heights (mm).

In order to understand this difference, we compared the $\delta^{18}O$ and δD values of thermal springs to that of rivers, groundwater and rain in both cirques (Figure 9.A) and monitored $\delta^{18}O$ and δD for two years in thermal springs IRN in Cilaos and TBA in Salazie and in rainfall at both sites (Figure 9.B). In Salazie, the distribution of $\delta^{18}O$ and δD values of thermal springs is very similar to that of rivers and groundwaters ($\delta^{18}O$ from -8.0 to -5.5 ‰ and δD from -46.1 to -33.0 ‰), indicating a similar recharge. In Cilaos, the only river sample available (rBRO, from this study) displays $\delta^{18}O$ and δD values (-7.18 and -44.4 ‰, respectively) in the range of that of thermal springs from Salazie and Cilaos, and that of rivers and groundwaters from Salazie. Additional data would thus be necessary to discuss $\delta^{18}O$ and δD values of rivers and groundwaters compared to thermal springs in the cirque of Cilaos. The range of $\delta^{18}O$ and δD isotopic ratios in rains is similar in Salazie and Cilaos expect for 2 data points with lower values in Cilaos corresponding to samples from cyclones (Figure 9).

We considered recharge by computing the volume-weighted mean $\delta^{18}O$ and δD isotopic ratios of rains over two years for each cirque (2017-2019), using our monthly monitoring data at both sites (Table 2). The weighted mean $\delta^{18}O$ and δD isotopic ratios in rainwater is much higher in the cirque of Salazie ($\delta^{18}O$=-5.94 ‰ and δD=-35 ‰, Figure 9) than in Cilaos ($\delta^{18}O$=-7.70 ‰ and δD=-50.4 ‰). A similar difference is also observed in the chronicles of rain analyses over the period 1985-1986 between Salazie ($\delta^{18}O$=-6.50 ‰ and δD=-37.6 ‰) and Cilaos (weighted mean $\delta^{18}O$=-7.23 ‰ and δD =-51.5 ‰, Grunberger, 1989). This difference is mostly visible during cyclones (Figure 9.B), which appear to constitute a low $\delta^{18}O$ and δD end-member with different values for Salazie and Cilaos. The $\delta^{18}O$ and δD dichotomy in thermal springs may thus be explained by a difference in the isotopic signature of the recharge by cyclones between the two cirques. We tentatively explain this contrast by the isotopic air

masses distillation at their passage over Piton des Neiges summit, from the windward slopes in Salazie to the leeward slopes in Cilaos. This strongly suggests that the Salazie and Cilaos hydrothermal reservoirs are not connected.

In comparison with rains, the two monitored thermal springs display very limited temporal $\delta^{18}O$ and δD variations (Figure 9.B). The Cilaos spring (IRN) is not only very stable (from -50.9 to -51.2 ‰, mean -51.0 ‰ for δD), but also very close to the volume-weighted mean $\delta^{18}O$ and δD isotopic ratios of rains in this cirque (-50.4 ‰ for δD, Figure 9.B). This stability holds over a ~20 year period with a δD value of -51.3 ‰ measured at IRN in 2000 by Sanjuan et al., (2001). $\delta^{18}O$ and δD values of the Salazie thermal spring (TBA) are also very stable over the two-year period (e.g. from -38.7 to -41.1 ‰, mean -40.2 ‰ for δD), and their mean is relatively close to the volume-weighted mean $\delta^{18}O$ and δD isotopic ratios of rains in this cirque (-35 ‰ for δD, Figure 9.B). This comparison of time series shows that thermal springs at these two sites are neither influenced by the seasonal variations of rains nor by mixing with shallow cold waters. The recharge, mostly influenced by important inputs of cyclonic water, is buffered by multi-year infiltration. This suggests that the Salazie and Cilaos hydrothermal reservoirs, although disconnected from each other, are sufficiently large and/or deep to be protected from superficial perturbations.

4.2.3. Host rock

In this section, we compared the $^{87}Sr/^{86}Sr$ in rocks and thermal waters to identify the geological units hosting the hydrothermal system. As with the $\delta^{18}O$ and δD isotopic ratios, we observe that $^{87}Sr/^{86}Sr$ ratios are higher in the thermal springs of Salazie (0.704194 to 0.704364, mean 0.704276 ± 0.000047) than in those of Cilaos (0.704129 to 0.704249, mean 0.704180 ± 0.000026), irrespective of Sr concentrations (Table 1, Figure 10), as already mentioned by Sanjuan et al., (2001). Because there is no fractionation between Sr isotopes during water-rock interaction, the strontium isotopic ratio is preserved when Sr is leached from the rock by thermal waters. This dichotomy thus reflects a difference between the two cirques in the $^{87}Sr/^{86}Sr$ ratios of rocks interacting with thermal fluids.

All rocks from Salazie and Cilaos (Table 3, Figure 10) fall in the range of $^{87}Sr/^{86}Sr$ ratios of thermal springs (from 0.704086 to 0.704290), except for two outliers in Salazie (0.704041 and 0.704504). However, our new analyses show that syenite intrusions, trachyte dykes and other differentiated products fall in the lower range of this $^{87}Sr/^{86}Sr$ isotopic diversity (from 0.704153 to 0.704269, mean 0.704181), whether they come from Salazie, Cilaos, or from the summit. The comparison of rock and thermal spring $^{87}Sr/^{86}Sr$ isotopic signatures thus strongly suggests that the hydrothermal fluids of Cilaos interact with differentiated rocks at low $^{87}Sr/^{86}Sr$ isotopic ratios whereas those from Salazie interact with more mafic rocks at higher $^{87}Sr/^{86}Sr$ isotopic ratios. Differentiated intrusions belong to the latest volcanic activity of Piton des Neiges (150 to 27 ka), and thus represent the likeliest heat sources in the edifice.

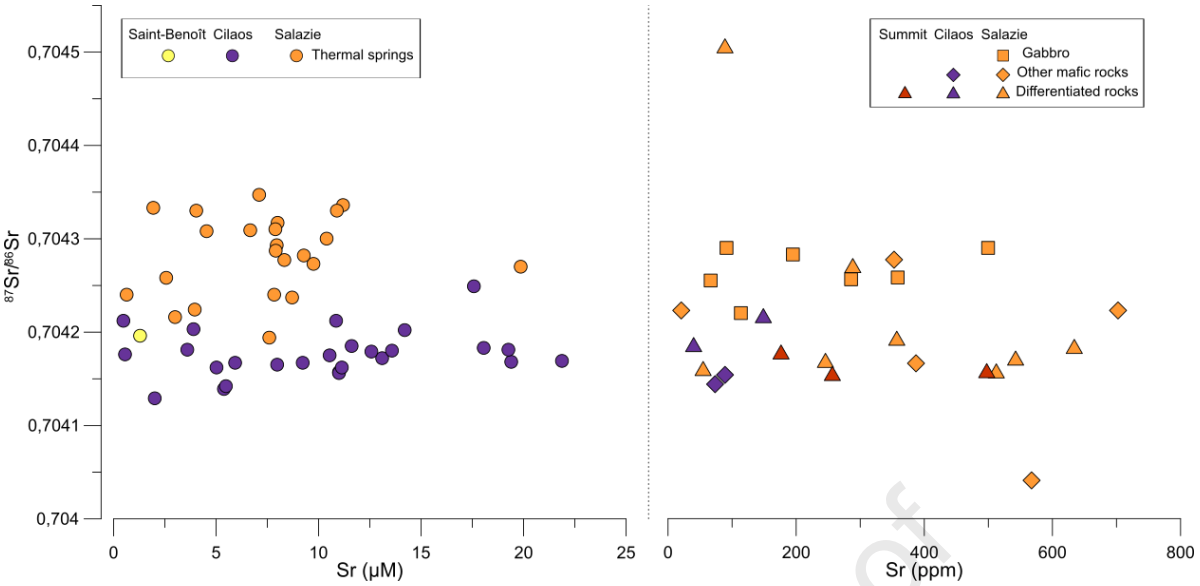

542

543 Figure 10: Strontium concentrations and $^{87}Sr/^{86}Sr$ isotopic ratios in thermal springs (µmol/L) and rocks (ppm) from
544 the cirques of Salazie and Cilaos.

545 Consequently, the contrasted $^{87}Sr/^{86}Sr$ values of thermal springs of Salazie and Cilaos implies that the
546 hydrothermal fluids interact with different rocks on the two sides of the summit. When combined with
547 the contrasted $\delta^{18}O$ and δD signatures of thermal springs (Figure 11) which show that meteoric
548 recharge is independent in the two cirques, we can deduce that the hydrothermal system is made of
549 two reservoirs that do not mix with each other. The Cilaos reservoir, which shows more evidence of
550 interaction with trachytes and syenites than the Salazie reservoir, is thus possibly closer to a heat
551 source related to the terminal activity of Piton des Neiges, and is therefore more promising from a
552 geothermal perspective.

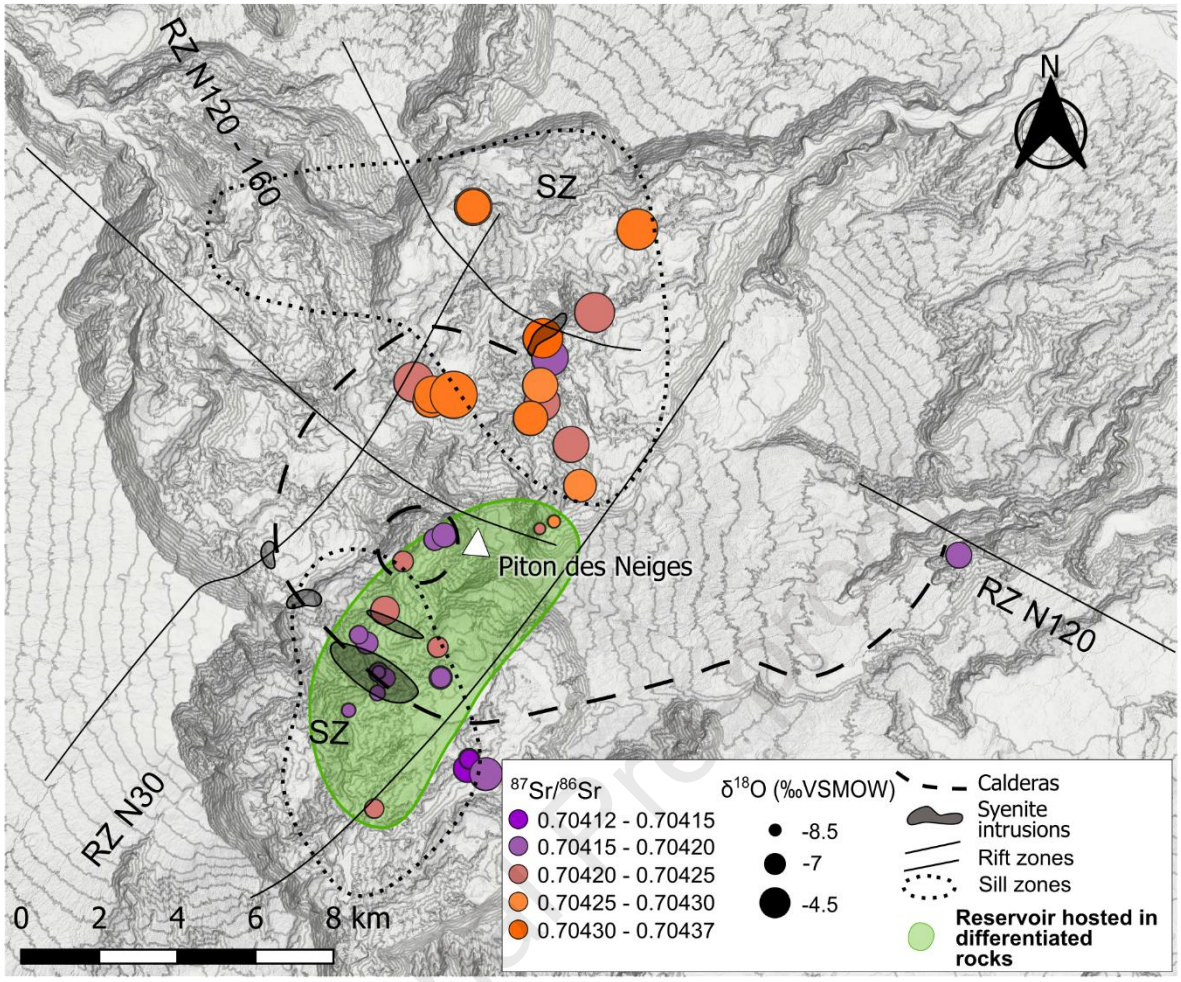

Figure 11: Spatial distribution of $\delta^{18}O$ (‰ VSMOW in symbol size) and $^{87}Sr/^{86}Sr$ (in color scale) in the thermal springs of Piton des Neiges. The green field represents the zone of lowest $^{87}Sr/^{86}Sr$ indicating an interaction of thermal waters with differentiated rocks, which may represent heat sources for the hydrothermal system. Volcano-tectonic structures (rift zones, sill zones, syenite intrusions, and calderas) are also represented.

4.3. Equilibration and geothermometry

The next step in the geochemical characterization of the resource is to provide a quantitative estimate of the temperatures at which thermal waters and rocks interact. In a previous study, Sanjuan et al., (2001) proposed a reservoir temperature reaching 120-130°C, based on empirical and semi-empirical geothermometers applied to the set of thermal springs known at that time. We now dispose of a wider set of analyses of thermal springs. We chose to start our geothermometry study by selecting the thermal springs most likely to have retained their reservoir characteristics. We then applied multicomponent geothermometry and fluid reconstruction with a thermodynamic approach on this selected subset of thermal springs to get an estimate of the reservoir conditions. The approach is summarized below and detailed in Appendix B.

We compared outlet temperatures to the results of geothermometers for rapidly adjusting equilibriums at low temperatures, such as K-Mg and amorphous silica systems (Fournier, 1977; Fournier and Potter, 1979; Giggenbach, 1988), to assess the equilibrium state of thermal waters. The closer the outlet temperature is to the temperatures obtained with these geothermometers, the more re-equilibrated the waters are. We also used the values of the outlet temperatures as indicators of the speed of transfer between the reservoir at depth and the surface. The higher the outlet temperatures

574 are, the faster the transfer and thus, the closer to reservoir conditions the waters are likely to be. Our
575 results show that the silica system is re-equilibrated for all springs, hence, equilibrium with silica will
576 have to be estimated for reservoir conditions in geothermometry computations. For the K-Mg systems
577 however, some springs are not fully re-equilibrated and may have retained some of their reservoir
578 characteristics. For geothermometry computation, we chose to select the five thermal springs that
579 displayed a > 20°C difference between their outlet temperatures and temperatures obtained with the
580 K-Mg geothermometer, as well as outlet temperatures higher than 25°C: BR16, BR17, RR1, TB and
581 OLIV2. Additionally, we selected thermal springs BR14 and BR12, whose K-Mg system are re-
582 equilibrated, but have the highest outlet temperatures (48.0 and 42.4°C, respectively). This selection
583 of analyses, based on outlet temperatures and geochemistry, corresponds to thermal springs found in
584 immediate vicinity of the syenite intrusions. This supports that syenite intrusions play the role as heat
585 sources and/or as drains channeling hydrothermal waters.

586 On these seven selected thermal springs, we performed multicomponent geothermometry using the
587 software iGeoT (Spycher and Finsterle, 2016), which couples the parameter estimation software
588 iTOUGH2 (Finsterle, 2007) with GeoT (Spycher et al., 2016). The principle is to find a temperature that
589 satisfies equilibrium between waters of a known composition and chosen reservoir minerals using
590 iterations of mass-balance/mass-action equations. Based on our previously acquired knowledge of the
591 hydrothermal system, we also modelled CO_2 loss and silica re-equilibration in our computations. For
592 thermal springs with several samples available (BR12, BR14, BR16, TB), the samples with the highest
593 equilibrium temperatures obtained with iGeoT are the less diluted, and hence those that we consider
594 as the most representative of reservoir conditions. The equilibrium temperatures obtained for this
595 selection of thermal springs are presented in Table 5. The uncertainties correspond to the T_{spread}
596 indicator of the iGeoT software, which gives the spread of log(Q/K) values for the selected minerals on
597 the temperature axis. Two examples of temperature estimations with iGeoT are shown in Figure 12
598 for the two highest temperatures obtained (springs BR12 and BR16).

599 Because the Na, K, and Ca activity ratios and the fugacity of CO_2 obtained with the model are all critical
600 parameters in the computation of the equilibrium temperatures, it is important to compare the results
601 of multi-equilibrium geothermometry with other geothermometers and geoindicators, such as those
602 from Fournier and Truesdell (1973), Giggenbach, (1984), and Cioni and Marini, (2020). The details of
603 this analysis are in section B.3 of the Supplementary material. We found that multi-equilibrium
604 geothermometry results are in discrepancy with the other geothermometers only for one sample of
605 spring BR14 and for three samples of spring BR16. In these samples, the equilibrium is likely disturbed
606 by an excess amount of CO_2 entering the system, which forces us to reject the temperatures deduced
607 from these analyses in our interpretation. For all the other samples, multi-equilibrium temperatures
608 and compositions obtained with iGeoT are in general consistency with other geothermometers and
609 geoindicators.

610 Table 5: Equilibrium temperatures obtained with geothermometry for selected analyses of thermal springs.

Thermal spring	**BR12**	**BR14**	**BR16**	**BR17**	**RR1**	**OLIV2**	**TB**
Location	Cirque of Cilaos					Cirque of Salazie	
Equilibrium temperature (°C)	139	136	141	124	135	93	125
Uncertainty (T_{spread}, °C)	8	13	29	20	19	27	12
Confidence	Good	Medium	Medium	Good	Good	Good	Good

611

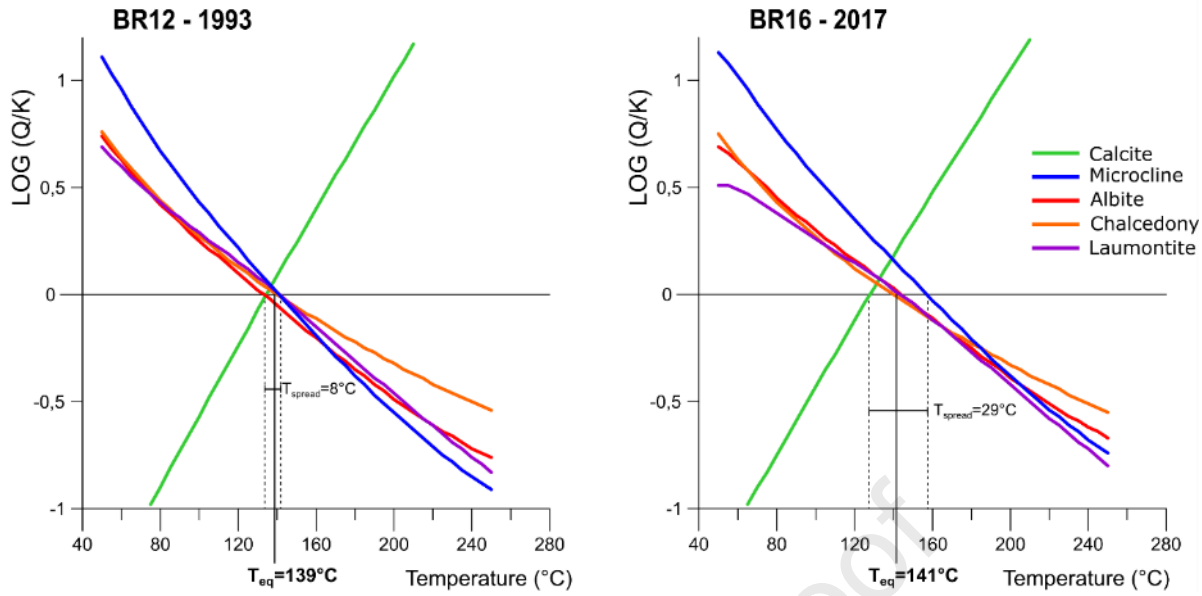

Figure 12: Examples of iGeoT computations on samples BR12 from Louvat and Allègre, (1997) and BR16 from Bénard et al., (2020), represented as saturation indices (log(Q/K)) of reservoir minerals versus temperatures. Q is the computed ion activity product with iGeoT and K the thermodynamic equilibrium constant of each mineral. The clustering of log(Q/K) curves near zero gives the reservoir temperature (T_{eq}), weighted to take into account the root-mean square, the standard deviation, the mean, and the scaled log(Q/K) absolute values. The uncertainty is the spread of log(Q/K) values (T_{spread}) for all minerals on the temperature axis.

Our multi-equilibrium geothermometry approach yields equilibrium temperatures from 93 ± 14°C to 125 ± 6°C (weighted mean 120 ± 5°C) for the two selected springs in the cirque of Salazie, and from 124 ± 10°C to 141 ± 15°C (weighted mean 137 ± 3°C) for the five springs in Cilaos (Table 5). These results are in general agreement with other geothermometers applied here and in Sanjuan et al., (2001, section B.3 of the Supplementary material). This consistency of multiple geothermometers suggests that the selected hydrothermal waters have reached equilibrium in their interaction with rock at the obtained temperatures. These springs are the ones most likely to have retained reservoir characteristics due to a fast transfer between the deep reservoir and the surface. It is important to note that this equilibrium is only the last one that the hydrothermal waters may have experienced, and that higher temperature equilibria may have occurred. In consequence, our results should be considered as minimum temperatures for the two independent hydrothermal systems of Salazie and Cilaos. Keeping this in mind, more thermal springs have reached equilibrium in Cilaos than in Salazie (5 against 2), and the Cilaos hydrothermal system appears to have reached slightly higher minimum temperatures than that of Salazie (Figure 13). In terms of geothermal resource, minimum equilibrium temperatures are thus more favorable in the cirque of Cilaos than in Salazie.

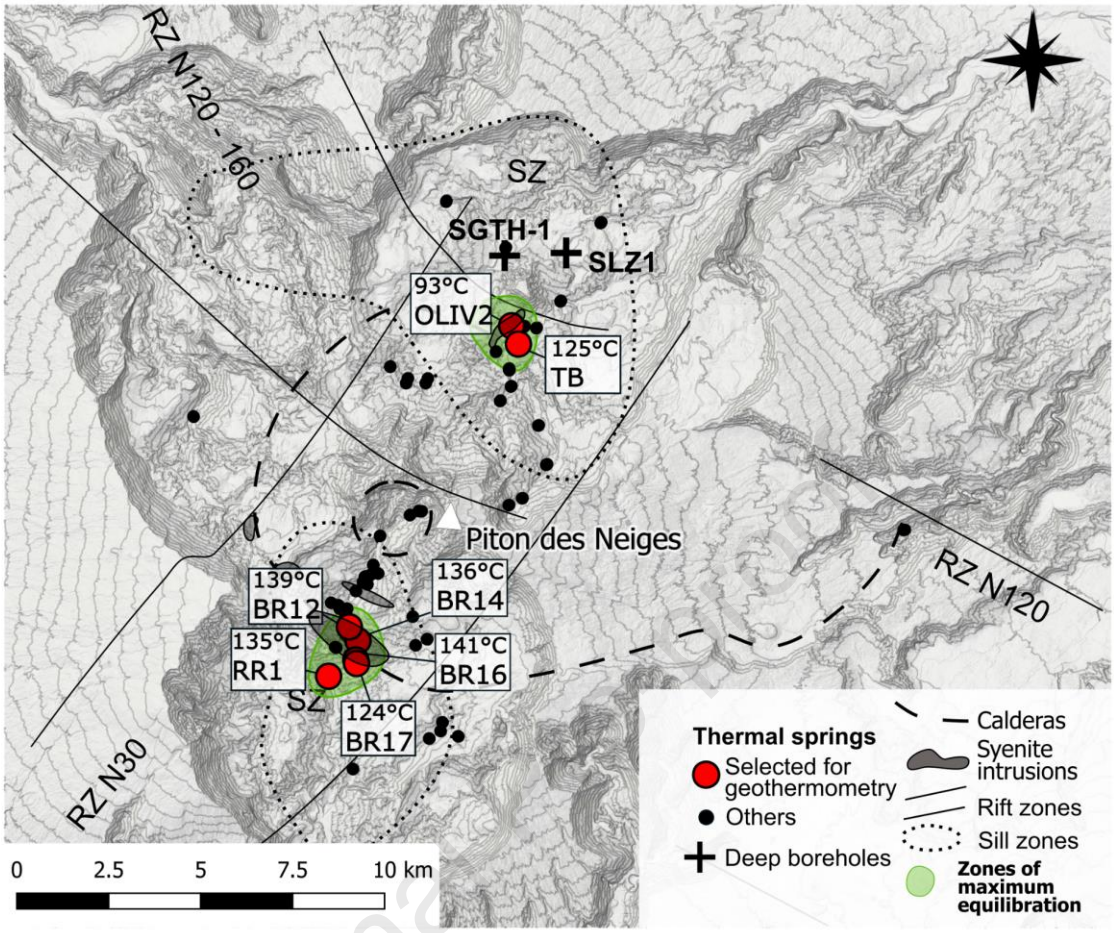

634

635 Figure 13: Spatial distribution of the thermal springs showing the best evidence of preserved high-temperature
636 equilibrium, and their multi-equilibrium temperature computed using iGeoT. relative to volcano-tectonic structures
637 (rift zones, sill zones, calderas). The green field represents the zone of highest equilibrium temperature of water-
638 rock interaction as defined in text. Volcano-tectonic structures (rift zones, sill zones, syenite intrusions, and
639 calderas) are also represented.

640 4.4. Geothermal resource

641 Our work has led us to identify zones where the geothermal resource appears to be the most promising
642 according to different criteria:

643 - 1. Maximum temperature and electrical conductivity in thermal springs,
644 - 2. Maximum degassing of CO_2,
645 - 3. Maximum contamination by seawater Cl, indicating that the hydrothermal system there is
646 deeply rooted,
647 - 4. Compartmented reservoir which is hosted in late stage differentiated rocks that could be a
648 heat source,
649 - 5. Most preserved equilibrium between thermal springs and the reservoir host rocks,
650 - 6. Minimum reservoir temperature of 130°C.

651 Figure 14 is a summary map superimposing all these six zones and thus giving the most probable
652 location of the geothermal resource. Two most promising zones are highlighted, one in the cirque of
653 Cilaos and the second is in the cirque of Salazie. This supports the observations made from the study

654 of the recharge and host rocks that there are two unconnected hydrothermal systems. These two
655 promising zones are located in the immediate surroundings of syenite intrusions, themselves located
656 at the junction of the N30°E rift zone and the supposed caldera of Piton des Neiges. This spatial
657 repartition clearly indicates that the differentiated magmas intruded in the N30°E rift zone during the
658 last activity of Piton des Neiges (150 – 27 ka, Famin et al., 2022), and to which the syenites belong,
659 represent the likeliest heat source of the two hydrothermal systems. The caldera structures and the
660 syenite intrusions could also represent preferential pathways for the ascent of hydrothermal fluids,
661 from a depth corresponding at least to the seawater level according to the slight contamination of
662 some springs by elements originating from seawater. The two hydrothermal systems appear large
663 and/or isolated enough to maintain a stable geochemical composition over several years.

664 The Cilaos zone is a more promising geothermal resource than the Salazie zone. This is partly due to
665 the higher average temperature obtained for the Cilaos reservoir (137 ± 3°C) compared to the Salazie
666 reservoir (125 ± 5°C). Additionally, the $^{87}Sr/^{86}Sr$ ratios of thermal springs from Cilaos, contrary to those
667 from Salazie, indicate that the thermal waters are interact with differentiated rocks that probably
668 constitute the heat source.

669 It is worth noting that in both cirques, the reservoir temperature estimates are below the limit of a
670 conventional energy-producing geothermal exploitation, which requires water at 150°C at the head of
671 the geothermal well (Moore and Simmons, 2013). We recall, however, that our estimates are minimum
672 temperatures of water-rock interaction, for hydrothermal waters that reach the surface. It is thus likely
673 that hotter hydrothermal waters exist at depth in the edifice, but either do not reach the surface or
674 are re-equilibrated at low temperature during their ascent.

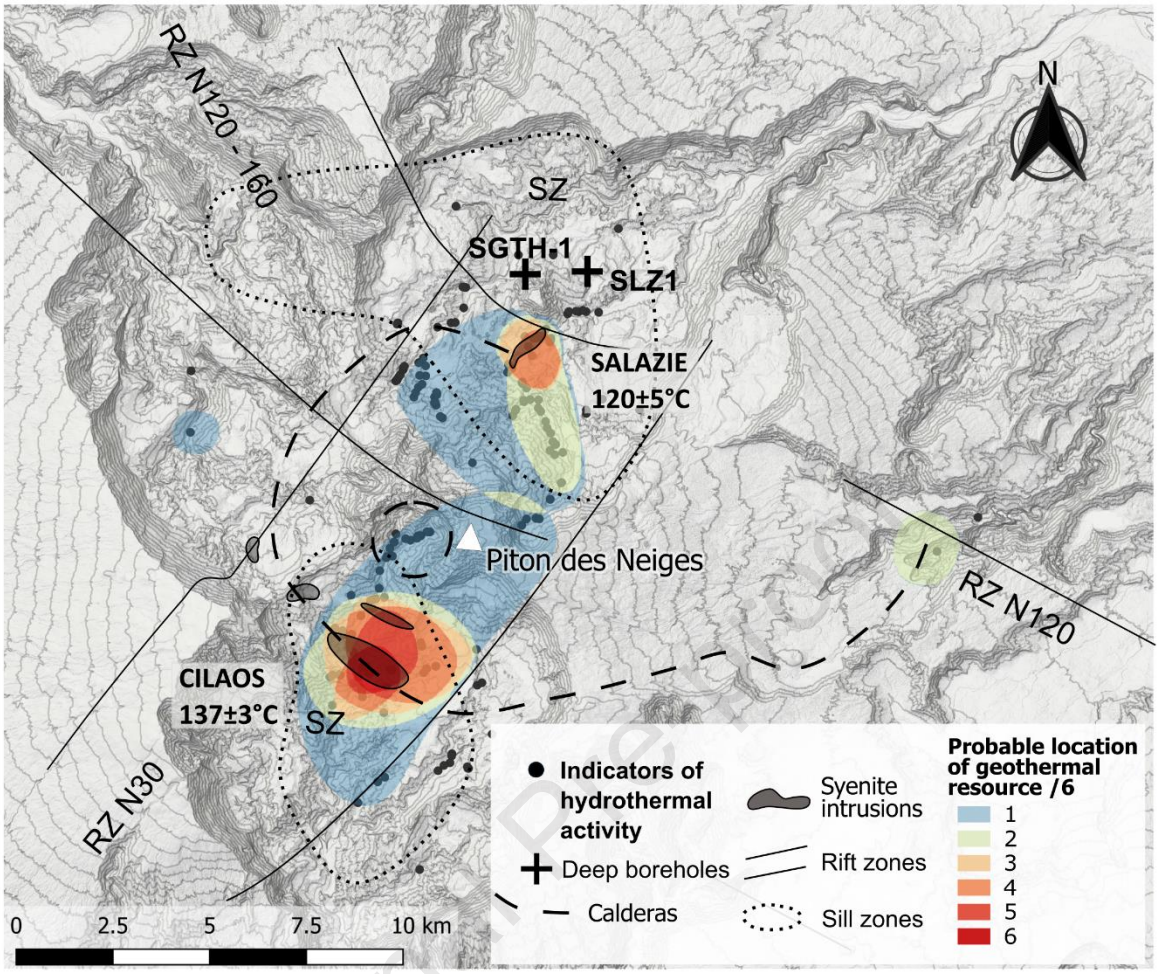

675

676 Figure 14: Superimposition of zones of: high temperature and electrical conductivity, high partial pressure of CO_2,
677 high seawater contribution relative other thermal springs (meaning that waters circulated deep), strontium isotopic
678 ratios corresponding to interaction with rocks from the late stage geological units, occurrence of thermal springs
679 equilibrated with their reservoir host rock, and equilibrium temperatures of water-rock interaction of thermal springs
680 superior to 130°C. The colors scale (/6) reflects how many zones are superimposed. The larger the number of
681 superimposed zones, the most probable it is that there is a geothermal resource.

682 ## Conclusion

683 Our vast exploration campaign and our extended dataset in space and time of major, trace elements
684 analyses and $\delta^{18}O$, δD, and $^{87}Sr/^{86}Sr$ isotopic ratios of thermal springs, rainwaters and rocks, allows us
685 to significantly precise the location of the geothermal resource of Piton des Neiges volcano, to estimate
686 a minimum temperature and to characterize its recharge. We show that the density of hydrothermal
687 indicators, including thermal springs and dry sulfur, iron oxide, and carbonate deposits, is dramatically
688 higher in the cirques of Salazie and Cilaos, along a N30°E axis corresponding to one of the volcanic rift
689 zones of the edifice. Dry deposits, particularly abundant on the northern extremity of this axis, may
690 represent the northern limit of hydrothermal activity. This may explain why previous investigation
691 boreholes located north of Salazie encountered heat but no sufficient water yield.

692 Contrasted $\delta^{18}O$, δD, and $^{87}Sr/^{86}Sr$ signatures in and Salazie and Cilaos thermal springs show that Piton
693 des Neiges hosts in fact two unconnected hydrothermal reservoirs, with independent meteoric
694 recharges and different water-rock interactions. For these two reservoirs, the most promising
695 geothermal resource in centered on syenite intrusions from the late stage magmatic activity. These

structures appear to be the likeliest heat source of hydrothermal activity, but also a preferential pathway for the upward circulation of hot fluids. Thermal springs in the vicinity of these zones keep a constant stable isotopic composition despite annual variations in rains. The recharge is multi-year, mostly due to cyclones and tropical storms. This buffering capacity indicates large aquifer volumes compared to annual infiltrations. The two hydrothermal aquifers display a slight seawater contamination, which suggest that hot fluids rise from depths equal to or greater than sea level. Multi-equilibrium geothermometry of selected thermal springs allow us to estimate a minimum temperature of 125 ± 5°C for the Salazie hydrothermal system, and a slightly higher minimum temperature of 137 ± 3°C for Cilaos.

Our spatial and temporal investigation of geochemical parameters in thermal springs lead us to considerably refine the characterization of the geothermal resource compared to previous studies. In particular, intersections of major volcano-tectonic structures such as the N30°E rift zones, the trace of the supposed caldera and syenites intrusions represent preferential targets for future investigations, which should prioritize the cirque of Cilaos.

Our spatial and temporal visualization of the geochemical information is thus well suited for geothermal exploration for geothermal systems with thermal springs strongly affected by mixing and re-equilibration. This geochemical exploration methodology is applicable to any volcano as long as the hydrothermal system leaks to the surface.

Acknowledgments

We thank Stefan Finsterle and Nicolas Spycher for guiding us with the use of the iGeoT program, and Jonas Greve and Victor K/Bidi for their participation in the fieldwork. We also thank the Établissement thermal de Cilaos for giving us access to their facilities and resources. The Ph.D. fellowship of B. Bénard was funded by Le Conseil Régional de La Réunion. This research has been supported by INSU-CNRS (project “STEAMRUN”) and OSU-Réunion (project “HYDROTHERM”) grants, by BRGM, by EDENA, and by IPGP multidisciplinary program PARI and Paris–IdF region SESAME (Grant no. 12015908).

References

Appelo, C.A.J., Postma, D., 2005. Geochemistry, Groundwater and Pollution, 2nd Edition. ed. A.A. Balkema Publishers.

Arnórsson, S., 1995. Geothermal systems in Iceland: Structure and conceptual models—II. Low-temperature areas. Geothermics 24, 603–629. https://doi.org/10.1016/0375-6505(95)00026-7

Assayag, N., Rivé, K., Ader, M., Jézéquel, D., Agrinier, P., 2006. Improved method for isotopic and quantitative analysis of dissolved inorganic carbon in natural water samples. Rapid Commun. Mass Spectrom. 20, 2243–2251. https://doi.org/10.1002/rcm.2585

Augé, T., Lerebour, P., Rançon, J.-P., 1989. The Grand Brûlé exploration drilling: New data on the deep framework of the Piton de la Fournaise volcano. Part 3: Mineral chemistry of the cumulate rocks. J. Volcanol. Geotherm. Res. 36, 139–151. https://doi.org/10.1016/0377-0273(89)90010-3

Aunay, B., Dewandel, B., Ladouche, B., Oliva, Z., Saussol, P., 2012. Identification des modalités d’exploitation des ressources en eaux souterraines du domaine d’altitude de l’Est de La Réunion – Phase 3 (secteur des Plaines) (Rapport final No. RP-59245-FR (http://infoterre.brgm.fr/rapports/RP-59245-FR.pdf)). BRGM.

Aunay, B., Gourcy, L., 2007. Approche hydrogéochimique pour la détermination de l’origine de la contamination des eaux. (No. RP-55535-FR http://infoterre.brgm.fr/rapports//RP-55535-FR.pdf). BRGM.

Aunay, B., Lucas, C., Ladouche, B., Vigouroux, P., Belle, P., 2013. Identification du potentiel en eau minérale gazeuse du cirque de Salazie (Rapport final No. RC-62181-FR). BRGM.

Ball, J.W., Nordstrom, D.K., 1991. User's manual for WATEQ4F, with revised thermodynamic data base and text cases for calculating speciation of major, trace, and redox elements in natural waters. US Geological Survey.

Belle, P., 2014. Contribution des processus hydrologiques et hydrogéologiques aux glissements de terrain de grande ampleur. Application au contexte tropical de La Réunion. Université de La Réunion, Saint-Denis, La Réunion.

Bénard, B., Famin, V., Agrinier, P., Aunay, B., Lebeau, G., Sanjuan, B., Vimeux, F., Bardoux, G., Dezayes, C., 2020. Origin and fate of hydrothermal fluids at Piton des Neiges volcano (Réunion Island): A geochemical and isotopic (O, H, C, Sr, Li, Cl) study of thermal springs. J. Volcanol. Geotherm. Res. 392, 106682. https://doi.org/10.1016/j.jvolgeores.2019.106682

Berthod, C., 2016. Relations entre systèmes intrusifs et instabilités sur un volcan basaltique (Piton des Neiges, La Réunion) (thesis). La Réunion.

Bird, D.K., Norton, D.L., 1981. Theoretical prediction of phase relations among aqueous solutions and minerals: Salton Sea geothermal system. Geochim. Cosmochim. Acta 45, 1479–1494. https://doi.org/10.1016/0016-7037(81)90280-5

Boudoire, G., Liuzzo, M., Di Muro, A., Ferrazzini, V., Michon, L., Grassa, F., Derrien, A., Villeneuve, N., Bourdeu, A., Brunet, C., Giudice, G., Gurrieri, S., 2017. Investigating the deepest part of a volcano plumbing system: Evidence for an active magma path below the western flank of Piton de la Fournaise (La Réunion Island). J. Volcanol. Geotherm. Res. 341, 193–207. https://doi.org/10.1016/j.jvolgeores.2017.05.026

Boudoire, G., Rizzo, A.L., Di Muro, A., Grassa, F., Liuzzo, M., 2018. Extensive CO 2 degassing in the upper mantle beneath oceanic basaltic volcanoes: First insights from Piton de la Fournaise volcano (La Réunion Island). Geochim. Cosmochim. Acta 235, 376–401. https://doi.org/10.1016/j.gca.2018.06.004

Bret, L., 2002. Minéralogie et géochimie des séries anciennes du Piton des Neiges : Modélisation et implications hydrogéologiques (Thèse). Université de la Réunion.

Chaput, M., Famin, V., Michon, L., 2017. Sheet intrusions and deformation of Piton des Neiges, and their implication for the volcano-tectonics of La Réunion. Tectonophysics 717, 531–546. https://doi.org/10.1016/j.tecto.2017.08.039

Chaput, M., Pinel, V., Famin, V., Michon, L., Froger, J.-L., 2014. Cointrusive shear displacement by sill intrusion in a detachment: A numerical approach. Geophys Res Lett 41 1937–1943.

Chevalier, L., 1979. Structures et évolution du volcan Piton des Neiges. Ile de la Réunion. Leurs relations avec les structures du bassin des Mascareignes. Océan indien occidental (Thèse). Université scientifique et médicale de Grenoble.

Chovelon, P., 1986. Forage géothermique de Salazie (SLZ1). Étude géologique du forage et dossier des ouvrages exécutés. (No. N°86CFG018).

Cioni, R., Marini, L., 2020. The Activity-Based Theoretical K–Ca and Na–Ca Geoindicators, in: Cioni, R., Marini, L. (Eds.), A Thermodynamic Approach to Water Geothermometry, Springer Geochemistry. Springer International Publishing, Cham, pp. 365–407. https://doi.org/10.1007/978-3-030-54318-1_8

Coudrain-Ribstein, A., Gouze, P., de Marsily, G., 1998. Temperature-carbon dioxide partial pressure trends in confined aquifers. Chem. Geol. 145, 73–89. https://doi.org/10.1016/S0009-2541(97)00161-7

Demange, J., Chovelon, P., Puvilland, P., 1989. Geothermal model of the Salazie Cirque (Reunion Island): Volcanic and structural implications. J. Volcanol. Geotherm. Res. 36, 153–176. https://doi.org/10.1016/0377-0273(89)90011-5

Dezayes, C., Famin, V., Tourlière, B., Baltassat, J.-M., Bénard, B., 2022. Potential areas of interest for the development of geothermal energy in La Réunion Island based on GIS analysis. J. Volcanol. Geotherm. Res. 421, 107450. https://doi.org/10.1016/j.jvolgeores.2021.107450

Di Paolo, F., Ledo, J., Slezak, K., Martínez van Dorth, D., Cabrera Pérez, I., Pérez, N., 2020. La Palma island (Spain) geothermal system revealed by 3D magnetotelluric data inversion. Sci. Rep. 10, 18181. https://doi.org/10.1038/s41598-020-75001-z

Dumont, M., Reninger, P.A., Pryet, A., Martelet, G., Aunay, B., Join, J.L., 2018. Agglomerative hierarchical clustering of airborne electromagnetic data for multi-scale geological studies. J. Appl. Geophys. 157, 1–9. https://doi.org/10.1016/j.jappgeo.2018.06.020

Famin, V., Berthod, C., Michon, L., Eychenne, J., Brothelande, E., Mahabot, M.-M., Chaput, M., 2016. Localization of magma injections, hydrothermal alteration, and deformation in a volcanic detachment (Piton des Neiges, La Réunion). J. Geodyn., Fluids in crustal deformation : fluid flow, fluid-rock interactions, rheology, melting and resources 101, 155–169. https://doi.org/10.1016/j.jog.2016.05.007

Famin, V., Paquez, C., Danišík, M., Gardiner, N.J., Michon, L., Kirkland, C.L., Berthod, C., Friedrichs, B., Schmitt, A.K., Monié, P., 2022. Multi-technique Geochronology of Intrusive and Explosive Activity on Piton des Neiges Volcano, Réunion Island. Geochem. Geophys. Geosystems n/a, e2021GC010214. https://doi.org/10.1029/2021GC010214

Finsterle, S., 2007. iTOUGH2 user's guide. Earth Sci. Div. Lawrence Berkeley Natl. Lab. Univ. Calif. Berkeley CA Httpwww-Esd Lbl GovTOUGHmanualsiTOUGH2GSLIBUsersGuide Pdf.

Fournier, R.O., 1977. Chemical geothermometers and mixing models for geothermal systems. Geothermics 5, 41–50. https://doi.org/10.1016/0375-6505(77)90007-4

Fournier, R.O., Potter, R.W., 1979. Magnesium correction to the Na□K□Ca chemical geothermometer. Geochim. Cosmochim. Acta 43, 1543–1550. https://doi.org/10.1016/0016-7037(79)90147-9

Fournier, R.O., Truesdell, A.H., 1973. An empirical Na-K-Ca geothermometer for natural waters. Geochim. Cosmochim. Acta 37, 1255–1275. https://doi.org/10.1016/0016-7037(73)90060-4

Frissant, N., Gourcy, L., Brach, M., 2005. Recherche d'une relation entre le plateau de Dos-d'Ane et les sources Blanche et Denise (No. RP-54167-FR (http://infoterre.brgm.fr/rapports/RP-54167-FR.pdf)). BRGM.

Frissant, N., Lacquement, F., Rançon, J.P., 2003. Etude du potentiel hydrothermal de la zone amont de la rivière du Bras Rouge (Cirque de Cilaos) -Première phase d'étude- (No. RP-52673-FR (http://infoterre.brgm.fr/rapports/RP-52673-FR.pdf)). BRGM.

Gérard, A., Stieltjes, L., 1979. Evaluation du potentiel géothermique de l'île de La Réunion. 2ème phase exploratoire: géologie et géophysique. (No. 79SGN538GTH).

Giggenbach, W.F., 1988. Geothermal solute equilibria. Derivation of Na-K-Mg-Ca geoindicators. Geochim. Cosmochim. Acta 52, 2749–2765. https://doi.org/10.1016/0016-7037(88)90143-3

Giggenbach, W.F., 1984. Mass transfer in hydrothermal alteration systems—A conceptual approach. Geochim. Cosmochim. Acta 48, 2693–2711. https://doi.org/10.1016/0016-7037(84)90317-X

Gillot, P.-Y., Nativel, P., 1982. K-Ar chronology of the ultimate activity of piton des neiges volcano, reunion island, Indian ocean. J. Volcanol. Geotherm. Res. 13, 131–146. https://doi.org/10.1016/0377-0273(82)90024-5

Grasby, S., Ansari, S., Calahorrano-Di Patre, A., Chen, Z., Craven, J., Dettmer, J., Gilbert, H., Hanneson, C., Harris, M., Liu, J., others, 2019. Geothermal Resource Potential of the Garibaldi Volcanic Belt, Southwestern British Columbia (Part of NTS 092J). Geosci. BC Summ. Act. 2020–02.

Grunberger, O., 1989. Etude géochimique et isotopique de l'infiltration sous climat tropical contrasté. Massif du Piton des Neiges. Ile de la Réunion (Thèse). Université de Paris XI.

Gudmundsson, B.T., Arnórsson, S., 2005. Secondary mineral–fluid equilibria in the Krafla and Námafjall geothermal systems, Iceland. Appl. Geochem. 20, 1607–1625. https://doi.org/10.1016/j.apgeochem.2005.04.020

Gunnlaugsson, E., Arnòrsson, S., 1982. The chemistry of iron in geothermal systems in iceland. J. Volcanol. Geotherm. Res. 14, 281–299. https://doi.org/10.1016/0377-0273(82)90066-X

Herrera, C., Custodio, E., 2014. Groundwater flow in a relatively old oceanic volcanic island: The Betancuria area, Fuerteventura Island, Canary Islands, Spain. Sci. Total Environ. 496, 531–550. https://doi.org/10.1016/j.scitotenv.2014.07.063

IAEA/WMO, 2019. Global Network of Isotopes in Precipitation. The GNIP Database. Accessible at: http://www.iaea.org/water.

Iundt, F., Mauroux, B., Barrera, L., Cruchet, M., Martignoni, P., Stieltjes, L., 1992. Etude des sources thermominérales de Cilaos (No. RR-35833-FR). BRGM.

Join, J.-L., Folio, J.-L., Robineau, B., 2005. Aquifers and groundwater within active shield volcanoes. Evolution of conceptual models in the Piton de la Fournaise volcano. J. Volcanol. Geotherm. Res. 147, 187–201. https://doi.org/10.1016/j.jvolgeores.2005.03.013

Jumaux, G., Queletard, H., Roy, D., 2011. Atlas climatique de la Réunion. METEOFRANCE.

Kluska, J.M., 1997. Evolution magmatique et morpho-structurale du Piton des Neiges au cours des derniers 500000 ans (Thèse). Université de Paris 11, Orsay.

Kristmannsdóttir, H., 1983. Chemical evidence from Icelandic geothermal systems as compared to submarine geothermal systems, in: Hydrothermal Processes at Seafloor Spreading Centers. Springer, pp. 291–320.

Kristmannsdottir, H., 1979. Alteration of Basaltic Rocks by Hydrothermal-Activity at 100-300°C, in: Mortland, M.M., Farmer, V.C. (Eds.), Developments in Sedimentology, International Clay Conference 1978. Elsevier, pp. 359–367. https://doi.org/10.1016/S0070-4571(08)70732-5

Lautze, N., Thomas, D., Hinz, N., Apuzen-Ito, G., Frazer, N., Waller, D., 2017a. Play fairway analysis of geothermal resources across the State of Hawaii: 1. Geological, geophysical, and geochemical datasets. Geothermics 70, 376–392. https://doi.org/10.1016/j.geothermics.2017.02.001

Lautze, N., Thomas, D., Waller, D., Frazer, N., Hinz, N., Apuzen-Ito, G., 2017b. Play fairway analysis of geothermal resources across the state of Hawaii: 3. Use of development viability criterion to prioritize future exploration targets. Geothermics 70, 406–413. https://doi.org/10.1016/j.geothermics.2017.07.005

Liuzzo, M., Di Muro, A., Giudice, G., Michon, L., Ferrazzini, V., Gurrieri, S., 2015. New evidence of CO2 soil degassing anomalies on Piton de la Fournaise volcano and the link with volcano tectonic structures. Geochem. Geophys. Geosystems 16, 4388–4404. https://doi.org/10.1002/2015GC006032

Lopoukhine, M., Stieltjes, L., 1978. Evaluation du Potentiel géothermique de l'Île de la Réunion - 1ère Phase exploratoire : Géologie et géochimie des eaux (No. 78 SGN 467 GTH). BRGM.

Louvat, P., Allègre, C.J., 1997. Present denudation rates on the island of Réunion determined by river geochemistry: Basalt weathering and mass budget between chemical and mechanical erosions. Geochim. Cosmochim. Acta 61, 3645–3669. https://doi.org/10.1016/S0016-7037(97)00180-4

Manès, G. (1871-) A. du texte, n.d. La Réunion : sanatoria, tourisme, livret-guide, illustré / par le docteur G. Manès,...

Marty, B., Meynier, V., Nicolini, E., Griesshaber, E., Toutain, J.P., 1993. Geochemistry of gas emanations: A case study of the Réunion Hot Spot, Indian Ocean. Appl. Geochem. 8, 141–152. https://doi.org/10.1016/0883-2927(93)90030-K

McDougall, I., 1971. The geochronology and evolution of the young volcanic island of Réunion, Indian Ocean. Geochim. Cosmochim. Acta 35, 261–288. https://doi.org/10.1016/0016-7037(71)90037-8

Mook, W.G., Koene, B.K.S., 1975. Chemistry of dissolved inorganic carbon in estuarine and coastal brackish waters. Estuar. Coast. Mar. Sci. 3, 325–336. https://doi.org/10.1016/0302-3524(75)90032-8

Moore, J.N., Simmons, S.F., 2013. More Power from Below. Science 340, 933–934. https://doi.org/10.1126/science.1235640

Nauret, F., Famin, V., Vlastélic, I., Gannoun, A., 2019. A trace of recycled continental crust in the Réunion hotspot. Chem. Geol. 524, 67–76. https://doi.org/10.1016/j.chemgeo.2019.06.009

Palandri, J.L., Reed, M.H., 2001. Reconstruction of in situ composition of sedimentary formation waters. Geochim. Cosmochim. Acta 65, 1741–1767. https://doi.org/10.1016/S0016-7037(01)00555-5

894 Pang, Z.-H., Reed, M., 1998. Theoretical Chemical Thermometry on Geothermal Waters: Problems and
895 Methods. Geochim. Cosmochim. Acta 62, 1083–1091. https://doi.org/10.1016/S0016-
896 7037(98)00037-4
897 Petit, V., Dewandel, B., Charlier, J.B., Ollivier, P., Lucas, C., Oliva, Z., 2013. Amélioration de la
898 connaissance hydrogéologique de l'aquifère côtier du Gol. (No. RP-61834-FR
899 http://infoterre.brgm.fr/rapports//RP-61834-FR.pdf). BRGM.
900 Poul, X., 1966. Les sources thermominérales de Cilaos étude géologique et étude des principales
901 caractéristiques : débit, température et résistivité-des captages existants. (No. 66- TAN- 027).
902 BRGM.
903 Rançon, J.P., Rocher, P., 1985. Découverte de zones fumerolliennes récentes dans le cirque de Salazie
904 (île de La Réunion, Océan Indien). C R Académie Sci. Sér. II 16, 821–826.
905 Rançon, J.Ph., 1985. Hydrothermal history of Piton des Neiges volcano (Reunion Island, Indian Ocean).
906 J. Volcanol. Geotherm. Res. 26, 297–315. https://doi.org/10.1016/0377-0273(85)90061-7
907 Reed, M., Palandri, J., 2006. SOLTHERM. H06, a database of equilibrium constants for minerals and
908 aqueous species. Available Authors.
909 Reed, M., Spycher, N., 1984. Calculation of pH and mineral equilibria in hydrothermal waters with
910 application to geothermometry and studies of boiling and dilution. Geochim. Cosmochim. Acta
911 48, 1479–1492. https://doi.org/10.1016/0016-7037(84)90404-6
912 Rocher, P., 1988. Contexte volcanique et structural de l'hydrothermalisme récent dans le massif du
913 Piton des neiges (île de La Réunion): étude détaillée du cirque de Salazie. s.n., S.l.
914 Sanjuan, B., Genter, A., Brach, M., Lebon, D., 2001. Compléments d'étude géothermique dans l'île de
915 la Réunion (géologie, géochimie) (No. RP-51189-FR (http://infoterre.brgm.fr/rapports/RP-
916 51189-FR.pdf)). BRGM.
917 Smietana, M., 2011. Petrology, geochronology (K-Ar) and elemental and isotopic geochemistry (Sr, Nd,
918 Hf, Pb) of older lavas of Reunion : Implications for the construction of the volcanic edifice
919 (Theses). Université de la Réunion.
920 Spycher, N., Finsterle, S., 2016. iGeoT v1.0: Automatic Parameter Estimation for Multicomponent
921 Geothermometry, User's Guide:
922 Spycher, N., Peiffer, L., Finsterle, S., Sonnenthal, E., 2016. GeoT User's Guide, A Computer Program for
923 Multicomponent Geothermometry and Geochemical Speciation, Version 2.1:
924 Troll, V.R., Carracedo, J.C., 2016. The geology of the Canary Islands. Elsevier.
925 Trull, T., Nadeau, S., Pineau, F., Polve´, M., Javoy, M., 1993. C-He systematics in hotspot xenoliths:
926 Implications for mantle carbon contents and carbon recycling. Earth Planet. Sci. Lett. 118, 43–
927 64. https://doi.org/10.1016/0012-821X(93)90158-6
928 Vesselinov, V.V., O'Malley, D., Frash, L.P., Ahmmed, B., Rupe, A.T., Karra, S., Middleton, R.S.,
929 Alexandrov, B., Mudunuru, M.K., Mims, M., Jameson, K., Sun, A., Scanlon, B., Banerji, A.,
930 Tartakovsky, D.M., Horne, R.N., Zhou, Z., Maguire, C., Skillman, S., Scharer, J., 2021. Geo
931 Thermal Cloud: Cloud Fusion of Big Data and Multi-Physics Models using Machine Learning for
932 Discovery, Exploration, and Development of Hidden Geothermal Resources. United States.
933 https://doi.org/10.2172/1782607
934

Declaration of interests

☒ The authors declare that they have no known competing financial interests or personal relationships that could have appeared to influence the work reported in this paper.

☐ The authors declare the following financial interests/personal relationships which may be considered as potential competing interests: